Ovarian cancer immunogenicity is governed by a narrow subset of progenitor tissue-resident memory T cells

Anadon, C.M.; Yu, X.Q.; Hanggi, K.; Biswas, S.; Chaurio, R.A.; Martin, A.; ... ; Conejo-Garcia, J.R.

Cancer Cell

Article

Ovarian cancer immunogenicity is governed by a narrow subset of progenitor tissue-resident memory T cells

Graphical abstract

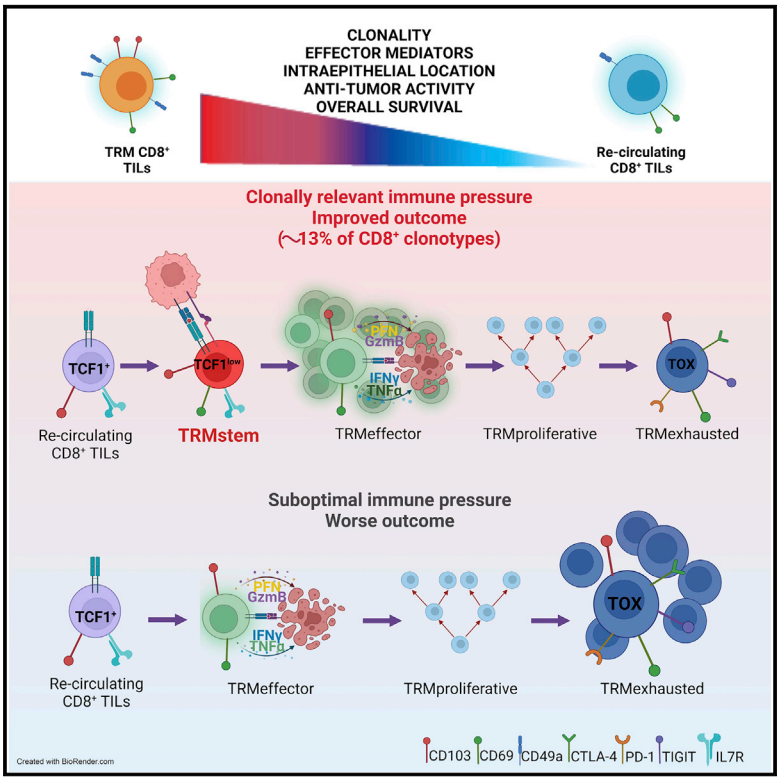

Highlights

- Only TRM TILs show clonal enrichment and effector activity in ovarian cancer
- Stem-like TRM cells replenish effector TRM cells as they become exhausted
- Intra-epithelial TCF1^{low} TRM TILs predict human ovarian cancer outcome
- Sustained ovarian cancer antigen recognition depends on ~13% of CD8$^+$ TILs

Authors

Carmen M. Anadon, Xiaoqing Yu, Kay Hänggi, ..., Robert M. Wenham, Paulo C. Rodriguez, Jose R. Conejo-Garcia

Correspondence

jose.conejo-garcia@moffitt.org

In brief

Anadon et al. demonstrate that human ovarian cancer-infiltrating T cells exhibiting hallmarks of sustained and active tumor antigen recognition are restricted to ~13% of CD8$^+$ T cells at tumor beds, corresponding to ~3% of CD8$^+$ clonotypes. These clonotypes represent TRM lymphocytes with a reservoir that retains features of stemness.

Anadon et al., 2022, Cancer Cell *40*, 545–557
May 9, 2022
https://doi.org/10.1016/j.ccell.2022.03.008

CellPress

Cancer Cell

CellPress
OPEN ACCESS

Article

Ovarian cancer immunogenicity is governed by a narrow subset of progenitor tissue-resident memory T cells

Carmen M. Anadon,[1] Xiaoqing Yu,[2] Kay Hänggi,[1] Subir Biswas,[1] Ricardo A. Chaurio,[1] Alexandra Martin,[3] Kyle K. Payne,[1] Gunjan Mandal,[1] Patrick Innamarato,[1] Carly M. Harro,[1] Jessica A. Mine,[1] Kimberly B. Sprenger,[1] Carla Cortina,[1] John J. Powers,[1] Tara Lee Costich,[1] Bradford A. Perez,[4] Chandler D. Gatenbee,[5] Sandhya Prabhakaran,[5] Douglas Marchion,[6] Mirjam H.M. Heemskerk,[7] Tyler J. Curiel,[8] Alexander R. Anderson,[5] Robert M. Wenham,[3] Paulo C. Rodriguez,[1] and Jose R. Conejo-Garcia[1,3,9,10,*]

[1]Department of Immunology, H. Lee Moffitt Cancer Center & Research Institute, 12902 Magnolia Drive, Tampa, FL 33612, USA
[2]Department of Biostatistics and Bioinformatics, H. Lee Moffitt Cancer Center & Research Institute, Tampa, FL 33612, USA
[3]Department of Gynecologic Oncology, H. Lee Moffitt Cancer Center & Research Institute, Tampa, FL 33612, USA
[4]Department of Radiation Therapy, H. Lee Moffitt Cancer Center & Research Institute, Tampa, FL 33612, USA
[5]Department of Mathematical Oncology, H. Lee Moffitt Cancer Center & Research Institute, Tampa, FL 33612, USA
[6]Department of Tissue Core, H. Lee Moffitt Cancer Center & Research Institute, Tampa, FL 33612, USA
[7]Department of Hematology, Leiden University Medical Center, Leiden, the Netherlands
[8]Department of Medicine, UT Health San Antonio, San Antonio, TX 78229, USA
[9]Department of Malignant Hematology, H. Lee Moffitt Cancer Center & Research Institute, Tampa, FL 33612, USA
[10]Lead contact
*Correspondence: jose.conejo-garcia@moffitt.org
https://doi.org/10.1016/j.ccell.2022.03.008

SUMMARY

Despite repeated associations between T cell infiltration and outcome, human ovarian cancer remains poorly responsive to immunotherapy. We report that the hallmarks of tumor recognition in ovarian cancer-infiltrating T cells are primarily restricted to tissue-resident memory (TRM) cells. Single-cell RNA/TCR/ATAC sequencing of 83,454 $CD3^+CD8^+CD103^+CD69^+$ TRM cells and immunohistochemistry of 122 high-grade serous ovarian cancers shows that only progenitor ($TCF1^{low}$) tissue-resident T cells (TRM_{stem} cells), but not recirculating $TCF1^+$ T cells, predict ovarian cancer outcome. TRM_{stem} cells arise from transitional recirculating T cells, which depends on antigen affinity/persistence, resulting in oligoclonal, trogocytic, effector lymphocytes that eventually become exhausted. Therefore, ovarian cancer is indeed an immunogenic disease, but that depends on ~13% of $CD8^+$ tumor-infiltrating T cells (~3% of $CD8^+$ clonotypes), which are primed against high-affinity antigens and maintain waves of effector TRM-like cells. Our results define the signature of relevant tumor-reactive T cells in human ovarian cancer, which could be applicable to other tumors with unideal mutational burden.

INTRODUCTION

A recurrent goal of cancer immunotherapy is to reinvigorate antigen-specific lymphocytes to promote their effector activity at tumor beds. While tumors promote metabolic paralysis of both activated and naive T cells (Cao et al., 2019; Song et al., 2018; Xia et al., 2017), immunotherapies blocking inhibitory immune checkpoints in tumor-reactive lymphocytes (Curiel et al., 2003) have recently transformed the outcome of multiple solid tumors (Baumeister et al., 2016).

After tumor antigen priming in lymph nodes, many tumor-reactive T cells acquire residency at peripheral tissues as tissue-resident memory (TRM)-like cells (Masopust and Soerens, 2019). TRM-like cells, typically co-expressing CD103 and CD69 (Dumauthioz et al., 2018), adapt to the metabolic demands of the tumor microenvironment (TME) (Ganesan et al., 2017; Pan et al., 2017), becoming crucial in both responses to immune checkpoint blockade (Ganesan et al., 2017; Siddiqui et al., 2019), and in spontaneous protective antitumor immunity (Bourdely et al., 2020; Dumauthioz et al., 2018; Malik et al., 2017; Molodtsov and Turk, 2018; Park et al., 2019; Savas et al., 2018).

Intratumoral stem-like $CD8^+$ T cells have also been found to be crucial drivers of immune pressure against established human tumors (Harjes, 2020; Jansen et al., 2019). At tumor beds, stem-like T cells expressing TCF1, previously identified as $TIM3^-IL7R^+CD8^+$ lymphocytes, coexist with exhausted ($PD1^+$ $TIM3^+$) lymphocytes (Hudson et al., 2019; Jansen et al., 2019). Significant overlap of the T cell receptor (TCR) in stem-like and terminally differentiated T cells has been identified, suggesting that stem-like tumor-infiltrating lymphocytes (TILs) could

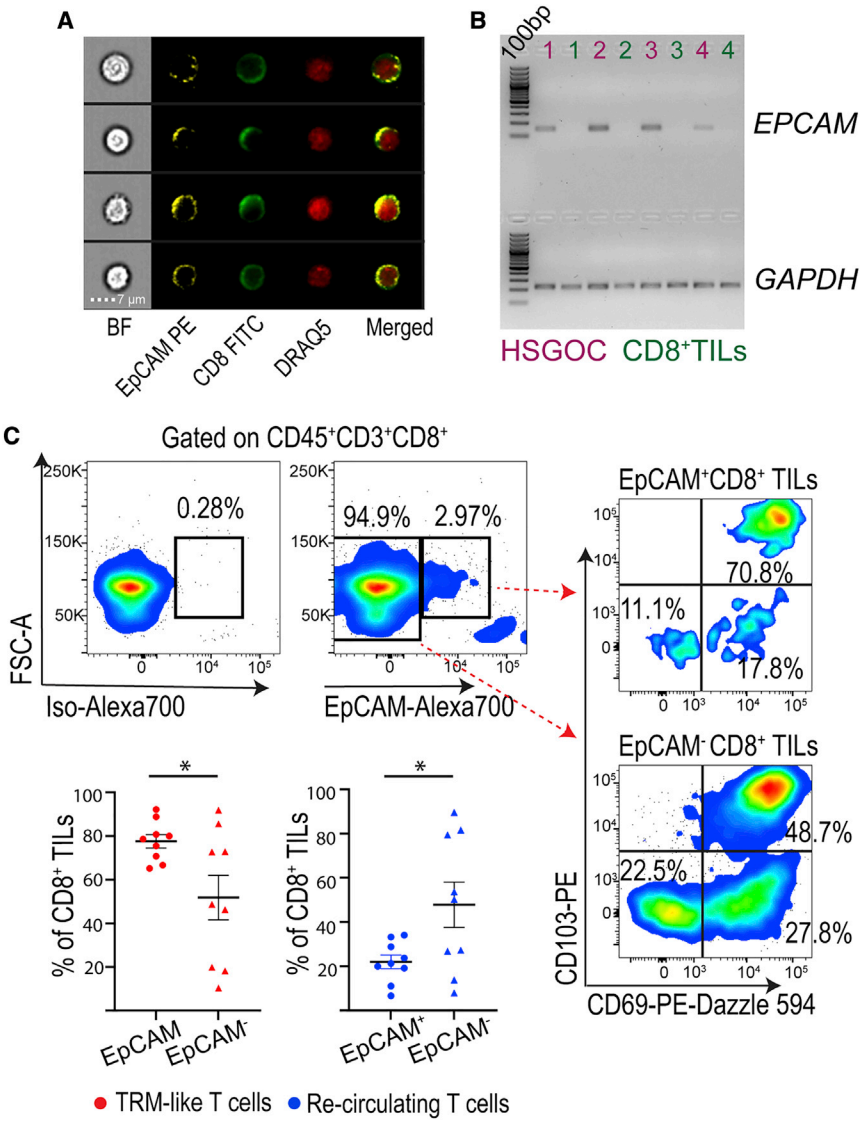

Figure 1. Analysis of trogocytosis in CD8⁺ TILs from HGSOC

(A) ImageStream multi-spectral images from a HGSOC showing CD8⁺ TILs including bright field (BF), EpCAM-PE (yellow), CD8-FITC (green), and DRAQ5 (red), and the merge showing the co-localization of CD8-EpCAM. Representative images shown from 200,000 total cells and 1,300 CD8⁺ analyzed.

(B) Agarose gel electrophoresis of *EPCAM* amplicons (150 bp) obtained by PCR amplification of cDNA from 4 different sorted CD8⁺ TILs paired to the tumors. *GAPDH* was used as the housekeeping gene.

(C) Dot plot of EpCAM⁺CD8⁺TILs from 18 HGSOC (top; representative image). Dot plot (right) and quantification (bottom) of the proportion of TRM-like CD8⁺ TILs (red) and recirculating CD8⁺ TILs (blue) within EpCAM⁺ CD8⁺TILs versus EpCAM⁻ TILs from 9 tumors with the presence of EpCAM⁺CD8⁺ TILs.

Data are presented as means with standard errors of the mean (SEM). Statistical analysis performed by paired t test (n = 9). *p < 0.05, **p ≤ 0.01, ***p ≤ 0.001.

See also Figure S1.

generate waves of effectors that eventually become exhausted (Harjes, 2020; Jansen et al., 2019). Recent evidence supports that these TIL populations are phenotypically similar to stem-like and exhausted T cells in chronic infections (Hudson et al., 2019; Jansen et al., 2019).

Although both TRM-like and stem-like TILs have been associated with immune protection, TRM cells typically lack the lymph node homing receptor CCR7 (Dumauthioz et al., 2018; Jadhav et al., 2019), which is usually expressed in *TCF7*⁺ lymphocytes (Siddiqui et al., 2019). In addition, TCF1, which drives T cell stemness (Wu et al., 2020), inhibits transforming growth factor β (TGF-β)-induced CD103 expression through binding to the gene locus, and *TCF7* (encodes TCF1)-deficient T cells accumulate as TRM lymphocytes in infection models (Wu et al., 2020). Accordingly, TCF1⁺PD-1⁺ stem-like and TRM-like TILs have been identified as clearly distinct populations, although stem-like lymphocytes could serve as TRM precursors (Siddiqui et al., 2019).

The failure of immune checkpoint blockade in ovarian cancer has recently placed in question the immunogenicity of this disease, despite quasi-universal consensus about the prognostic value of T cell infiltration. Initially using trogocytosis, a bidirectional process by which immune and target cells extract membrane proteins from each other (Joly and Hudrisier, 2003), as a signature of TCRs actively recognizing tumor antigen, the goal of this study was to define the existence and nature of TILs actively recognizing tumor antigens in human ovarian cancer patients. We reported that protective T cell immunity against ovarian cancer depends on a narrow subset of clonotypes with the capacity to form a reservoir of stem-like TRM-like cells.

RESULTS

TRM-like CD8⁺ TILs show signs of trogocytosis, recognize different antigens than recirculating CD8⁺ T cells, and exhibit superior antitumor activity

To identify TILs that indisputably recognize tumor antigens, we focused on CD8⁺ T cells exhibiting signs of trogocytosis-induced transfer of EpCAM protein from ovarian cancer cells. Fluorescence-activated cell sorting (FACS) analysis and multi-spectral imaging flow cytometry of single-cell suspensions from 18 different freshly dissociated high-grade serous ovarian carcinomas (HGSOC) revealed that in 9 of them, the membrane of 1%–4% of CD3⁺CD8⁺ singlets co-stained with EpCAM, an epithelial marker that is not detected at the mRNA level in T cells (Figures 1A, 1B, and S1A). Interestingly, EpCAM⁺ TILs also expressed CD103 and CD69 (Figure 1C), phenotypic

markers associated with TRM-like T cells, which predict better survival in ovarian cancer (Webb et al., 2014). These cells co-expressed CD49a and represented ~60% of $CD8^+$ TILs infiltrating 7 freshly dissociated HGSOC (Figures 2A, S1B, and S1C).

To identify other hallmarks of TRM lymphocytes, we compared the transcriptional profile of $CD3^+CD8^+CD103^+CD69^+CD49a^+$ TRM-like cells versus recirculating ($CD3^+CD8^+CD103^-$) T cells sorted from the same tumors (Figures 2A and S1D). Compared to recirculating TILs, TRM-like cells expressed >287 genes with significantly different mRNA abundance (Figures 2B, S1E, and S1F). These cells exhibit the transcriptional profile of TRM cells reported by independent authors (Figure S1G) (FitzPatrick et al., 2021; Mackay et al., 2013; Milner et al., 2017; Wakim et al., 2012). These included, for instance, the transcription factors RBPJ and EOMES (Mackay et al., 2016; Oja et al., 2018). As reported (Blank et al., 2019; Hartana et al., 2018), TRM-like cells showed higher expression of T cell exhaustion markers such as *PDCD-1*, *LAYN*, *CTLA4*, *TIGIT*, *TOX*, and *HAVCR2* (Figures 2B, S1E, and S1F), suggestive of prolonged exposure to cognate antigen. TRM-like cells also exhibited a higher expression of effector mediators, including *IFNG* and *GZMB*, but lower levels of stemness markers, such as *TCF7*, *IL7R*, *LEF1*, *CCR7*, and *CD28* (Hudson et al., 2019; Jansen et al., 2019). TRM-like cells also overexpressed *CXCL13*, associated with B cell recruitment and neoantigen burden in human malignancies (Workel et al., 2019), and *CXCR6*, encoding the receptor for CXCL16, quasi-universally overexpressed in ovarian cancer (Zsiros et al., 2015) (Figures 2B, S1E, and S1F). Further supporting repeated antigen engagement by TRM-like TILs, differential pathway analysis identified a mitotic cell-cycle progression signature, along with features of clonal expansion and exposure to tumor hypoxia, compared to their recirculating counterparts (Figures 2C, S1H, and S1I).

To confirm that tumor-reactive T cells reside in the TRM-like compartment, we analyzed TCR repertoires of TRM-like versus recirculating $CD8^+$ TILs from 12 different HGSOCs. On average, <12.5% of TCR-beta chains were shared between the TRM-like and the recirculating $CD8^+$ T cell compartments (Figure 2D). As expected, TRM-like TILs showed higher clonality (dominance of proportionally fewer clones; Figure 2E).

To functionally validate the protective role of TRM-like T-cells *in vivo*, we transferred (intratumorally, to bypass defective trafficking to tumor beds), ovalbumin (OVA)-specific OT-I T cells into flank (p53/KRas-dependent) OVA^{low}-UPK10 ovarian tumors developed in congenic mice (Rutkowski et al., 2015; Scarlett et al., 2012; Zhu et al., 2016) (Figure 2F). After 7 days, ~40% of tumor antigen-specific TILs acquired a TRM-like phenotype, while the rest remained as $CD103^{neg}$ (recirculating) lymphocytes (Figure 2G), which were also found in blood (Figure S1J). TRM-like formation depended on encounters with antigens because unprimed OT-I cells could not acquire TRM-like features in OVA^{neg} tumors (Figure 2H), while T cell activation before intratumoral administration greatly enhanced the accumulation of $CD8^+CD103^+CD69^+$ TILs (Figures 2H and S1K). Most important, $CD103^+CD69^+$ tumor antigen-specific TRM-like TILs recovered from dissociated tumors were more effective than their $CD103^{neg}$ OT-I counterparts at delaying the growth of different OVA^{low} tumors, although both subsets had remained in the same TME for the same period of time (Figure 2I). Similar results were obtained using Pmel T cells and gp100-UPK10 tumors (Figure 2J), supporting the notion that the TRM-like phenotype equips tumor-reactive T cells for a superior antitumor response. Together, these results indicated that TRM-like and recirculating TILs exhibit different phenotypes and clonotypes in human ovarian cancer, with all of the hallmarks of tumor reactivity primarily found in TRM-like T cells, which also exhibit superior antitumor activity at tumor beds.

Clonal TRM-like TILs show a trajectory of differentiation from stem-like cells to truly exhausted T cells

To further characterize TIL heterogeneity, we performed single-cell RNA sequencing (scRNA-seq) paired to VDJ profiling with 19,193 $CD103^+$ $CD69^+CD8^+$ TRM-like and 24,175 recirculating T cells sorted from 4 different HGSOCs. We identified 28 clusters in 5 major groups according to gene expression profile and TCR similarity (Figures 3A and S2A–S2F). After scoring stemness and exhaustion (Figure S2G), plus the transcriptional profile of TILs sharing the same TCR, we identified a trajectory of differentiation of $CD103^+CD69^+$ TRM-like cells, from a recently activated $CD103^-CD69^+$ recirculating population that turns into $TCF7^{low}$ $IL7R^+CCR7^+CD38^-$ lymphocytes, which retain features of stemness (TRM_{stem}). These "stem-like" cells differentiate into $GZMB^+PRF1^+GNLY^+ZNF683^+$ effector TRM-like T cells (TRM_{eff}), and then into $TIGIT^{low}HAVCR2^{+/low}$ HLA-$DR^{high}ENTPD1^{+/low}$ TOX^+ TILs with a highly proliferative signature (TRM_{prol}; Figure S2H), before turning into truly exhausted $PD\text{-}1^{high}$ $HAVCR2^{high}TIGIT^{high}ENTPD1^{high}$HLA-$DR^+TOX^+$ cells (TRM_{exh}) (Figures 3A, 3B, S2B, and S2I–S2K). In contrast, the recirculating T cells do not parallel the evolution of TRM-like TILs (Figure S2L).

Corresponding expression of selected proteins was confirmed by flow cytometry in different tumors (Figures S3A–S3C). This trajectory was supported by the enrichment of specific gene sets (Figure S3D) and was further confirmed through the simultaneous profiling of gene expression (nuclear RNA) and open chromatin (assay for transposase-accessible chromatin [ATAC]) from the same cell (Figures S3E and S3F), which shows parallel nuclear RNA expression and enriched peaks and gene activity at these loci (Figures 3B–3E and S3F). These concurrent analyses unveiled multiple modules of co-regulated genes, including genes associated with T cell stemness (*IL7R*, *CD28*, *CCR7*, *CD27*, *CXCR5*), mediators associated with T cell effector activity (*GZMB*, *GNLY*, *PRF1*, *IFNG*), programs linked to T cell proliferation (*STMN1*, *MCM7*, *TOP2A*, *CDK1*, *DNMT1*), and molecules associated with T cell exhaustion/dysfunction (*PDCD1*, *HAVCR2*, *TIGIT*, *CTLA4*). We also identified novel markers differentially expressed in specific TRM-like subsets. For instance, our analysis unveiled gradual increases in the expression of *ETV1* throughout $TRM_{eff} \rightarrow TRM_{prol} \rightarrow TRM_{exh}$ differentiation. In contrast, *GZMK* expression levels were maximal in TRM_{stem} cells and progressively decreased during the process of exhaustion (Figures 3B and S3F). This analysis also showed an enrichment of zinc finger DNA-binding domains *(ZNF*, *KLF*, *SP)* in TRM_{stem} cells, while motifs associated with nuclear receptors and homeodomains such as POU domains were enriched in more differentiated TRM-like subsets, with FOX and HOX domains increased in TRM_{exh} cells (Figure 3F).

Further scVDJ profiling/RNA-seq analysis showed that ~13% of TCRs in recently activated ($CD69^+$) recirculating ($CD103^-$)

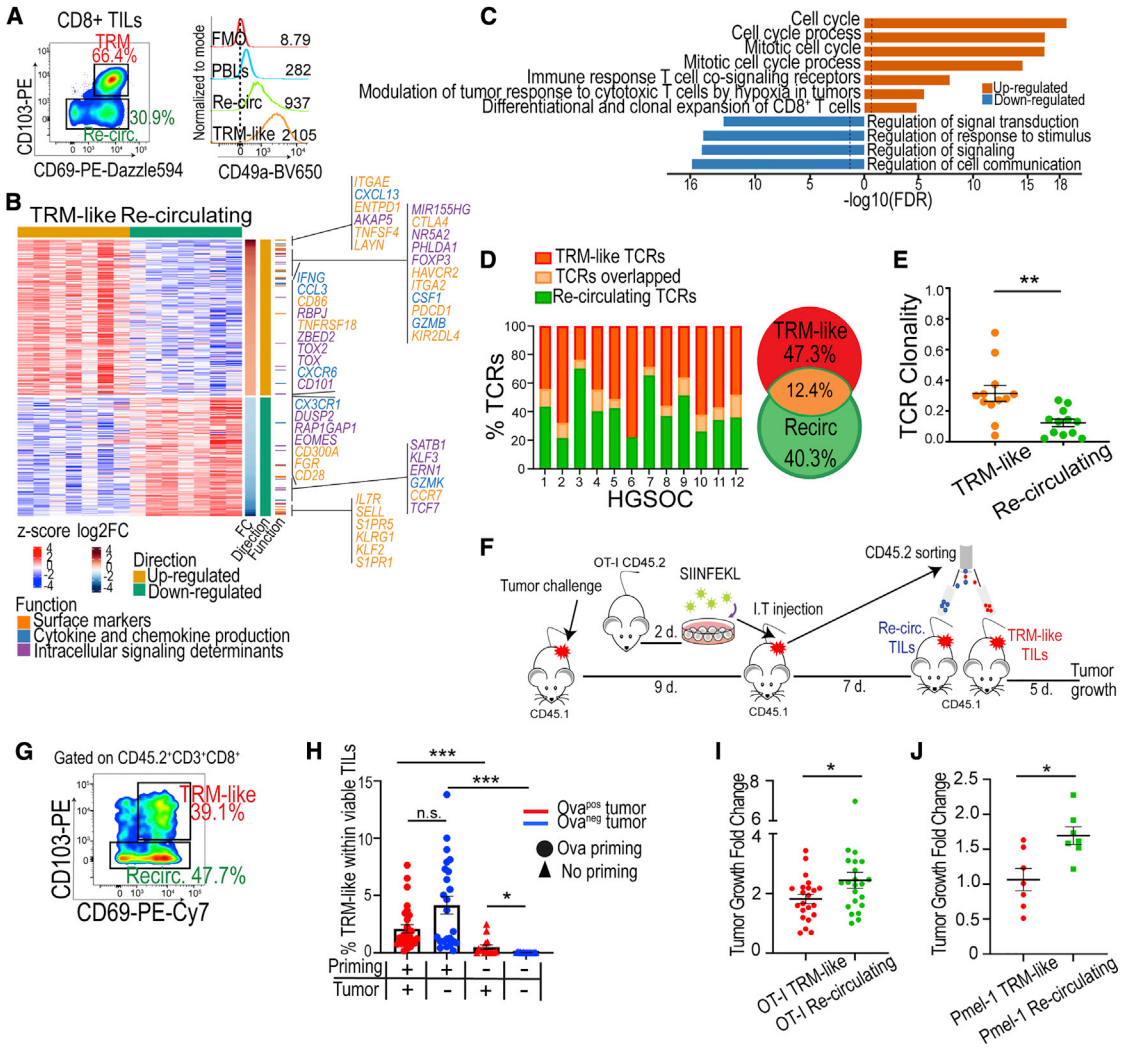

Figure 2. Hallmarks of active tumor recognition are found on TRM-like CD8⁺ TILs, but not in their recirculating counterparts

(A) Dot plot (left panel) of the proportions of TRM-like and recirculating CD8⁺ TILs in HGSOC. Representative dot plot shown from seven tumors. Histograms (right panel) show the expression of CD49a (MFI shown).

(B) Heatmap showing differentially expressed genes between TRM-like vs re-circulating CD8⁺ TILs sorted from 7 HGSOCs. Genes with log2-fold change >1 (fold change > 2) and false discovery rate (FDR) controlled $p < 0.05$ (N = 163) were considered upregulated. Genes with log2-fold change < −1 and FDR-controlled $p < 0.05$ (N = 124) were considered downregulated. Signature genes are labeled by function.

(C) Gene Ontology (GO) enrichment analysis for differentially expressed genes in TRM-like versus recirculating CD8⁺ TILs from the same tumors. Bar plot shows −log10(p value) of the pre-ranked gene set enrichment analysis (see STAR Methods).

(D) TCR-β repertoire of sorted TRM-like and re-circulating CD8⁺ TILs from 12 HGSOCs. Bar plot (left) shows the percentage of unique TCRs and overlapped TCRs in TRM-like versus recirculating CD8⁺ TILs in each tumor. Venn diagram (right) shows the average of unique TCRs in TRM-like (red), recirculating (green), and overlapped TCRs (orange) among the 12 tumors.

(E) Productive clonality (Shannon entropy). Data show means with SEMs Paired t test. *$p < 0.05$, **$p \leq 0.01$, ***$p \leq 0.001$.

(F) Experimental setting.

(G) Representative FACS dot plot of TRM-like and recirculating CD8⁺ TILs obtained from OVA^{low}-UPK10 tumors, 7 days after purified CD8⁺ OT-I T cells were injected intratumorally, *ex vivo* activated 2 days prior.

(H) Percentage of recovered TRM-like from UPK10 tumors transduced with OVA^{low} (red) or empty vector (mock, blue) 7 days after intratumoral injection of purified CD8⁺ OT-I T cells, activated 2 days prior with SIINFEKL or maintained with IL-2 (control). Pooled from 5 independent experiments.

(I) Fold change of OVA^{low}-UPK10 tumor volume 5 days after injection with TRM-like or recirculating TILs sorted from OVA^{low}-UPK10 tumors, injected 7 days before with purified, SIINFEKL-activated, CD8⁺ OT-I cells. Pooled from 3 independent experiments.

(J) Fold change of gp100-UPK10 tumor volume 5 days after injection with TRM-like or recirculating TILs sorted from gp100-UPK10 tumors, injected 7 days before with purified Gp100(25-33)-activated CD8⁺ Pmel cells. Pooled from 3 independent experiments.

For (H–J), the data presented show means with SEMs Each dot represents 1 mouse. Unpaired t test non-parametric (Mann-Whitney test). *$p < 0.05$, **$p \leq 0.01$, ***$p \leq 0.001$.

See also Figure S1 and Table S1.

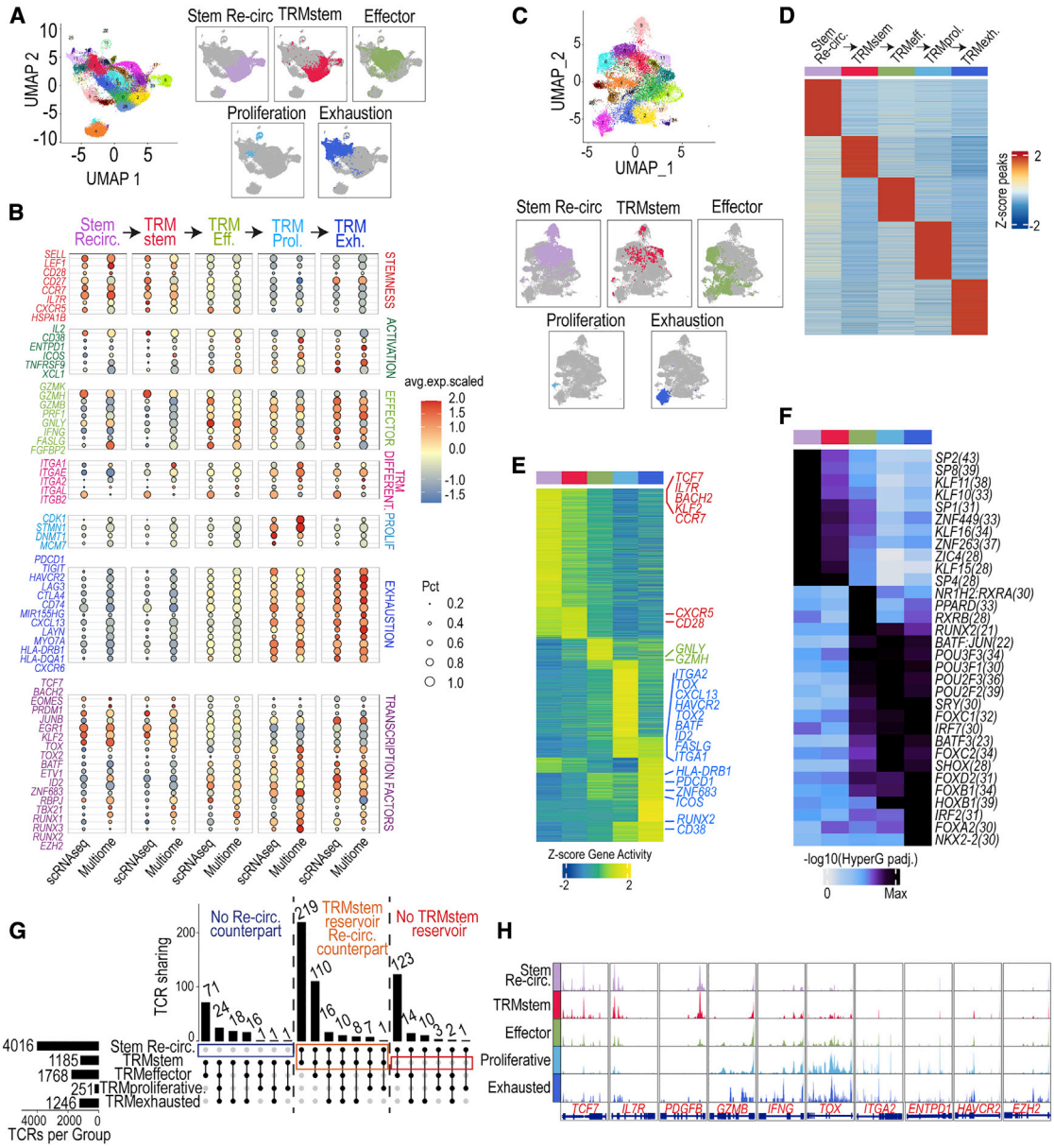

Figure 3. Matched single-cell gene profile and single-cell chromatin accessibility analysis reveal a trajectory of differentiation from TRM_{stem} cells to TRM_{exh} TILs

(A) Left: Uniform manifold approximation and projection (UMAP) of 24,175 recirculating TILs and 19.193 TRM-like $CD8^+$ TILs sorted from 4 HGSOCs showing 27 colored clusters. $CD3^+CD8^+CD103^-$vs $CD3^+CD8^+CD103^+$ $CD69^+CD49a^+$ TILs were sorted and sequenced separately and then merged for analysis. Each dot represents 1 unique cell. Right: Cells are colored by 5 major groups.

(B) Relative expression bubble plot of selected genes known to be associated with different stages of TRM-like differentiation. The color of each dot represents the average normalized expression from high (red) to low (blue). The size of each dot represents the percentage of positive cells for each gene.

(C) UMAP projection of 4,251 TRM-like and 16,615 re-circulating TILs sorted from 4 HGSOCs showing 22 color-coded cell clusters, using chromatin accessibility and nuclear RNA data (top), or the major 5 cell class annotations (bottom).

(D–F) Heatmap of class-specific (D) peaks, (E) gene activity scores, and (F) TF motifs enriched in peaks. Each column represents 1 group of the trajectory of the TRM-like differentiation. Each row represents differentially accessible peak regions (N = 57,555) (D), genes showing differential activity across the major groups (E) and transcription factor motifs (F). For (D and E), color represents row-wise z-transformed average scores with values thresholded at −2 and +2 for each peak and gene. For (F), the color represents normalized enrichment (−log10(FDR adjusted p value) of the TF motifs within the differentially accessible peaks of each major group.

(G) TCR sharing between the 5 major groups obtained by single-cell VDJ profiling. The bar on the left shows the number of unique clonotypes in each group. The bar in the top panel shows the number of clonotypes shared for the groups with a black dot under the bar.

(H) Normalized scATAC-seq-derived pseudo-bulk accessibility tracks of specific genes showing unique chromatin accessibility profiles for each major group. Tracks are normalized to the total number of reads aligned to transcription start site (TSS) regions.

See also Figures S2–S4 and Tables S2 and S3.

T cells were shared with TRM-like TILs, while 9.2% were expressed by TRM_{stem} cells (Figure 3G; Table S2). These recirculating cells exhibit a distinct transcriptional profile, compared to other recirculating lymphocytes, supportive of a transitional phenotype between recent priming and tissue residency differentiation (Figure S4A). Accordingly, we also identified clonotypes that lack a recirculating counterpart, suggestive of older priming and complete TRM-like differentiation (Figures 3G and S4B–S4E). As expected, 24% of TRM_{stem} clones shared TCRs with other TRM-like clusters. However, 35% of TILs in these samples differentiated into TRM_{eff} and TRM_{exh} cells without a TRM_{stem} pool (Figure 3G; Table S2). Accordingly, TRM_{exh} lymphocytes, but not other TRM-like cells, exhibited the typical chromatin signature and *HAVCR2/TOX/ENTPD1/CTLA-4* expression of truly exhausted T cells (Khan et al., 2019; Pauken et al., 2016) (Figures 3H and S4J). A total of 16% of TCRs shared between TRM_{exh} cells and other non-stem TRM-like lymphocytes were also found in TRM_{stem} cells, which showed no signs of exhaustion in their chromatin and ATAC-seq profiles, similar to stem-like T cells in infection models (Jadhav et al., 2019) (Figure 3H).

TRM_{stem} TILs, but no $TCF1^{+}CD103^{neg}$ TILs, predict the outcome of patients with ovarian cancer

To independently confirm the $TRM_{stem} \rightarrow TRM_{eff} \rightarrow TRM_{prol} \rightarrow TRM_{exh}$ trajectory of differentiation, and to gain additional insight into the heterogeneity of TRM-like TILs in ovarian cancer, we conducted additional scRNA-seq (cytoplasmic + nuclear), coupled to VDJ profiling, with 60,010 TRM-like $CD8^{+}$ T cells from 8 HGSOCs (Figures 4A and S5). Overall, they expressed typical genes of TRM-like cells previously published for other groups (Figure S5B). As expected (Wu et al., 2020), $TCF1^{+}$ TRM_{stem} cells exhibited lower TGF-β-dependent CD103 expression (Figures 4B, 4C, and S5D), compared to other TRM-like subsets. However, they also expressed markers of TRM-like differentiation, including *ITGA1* (encodes CD49a), *RUNX3*, plus *ITGAL* and *ITGB2*, which encode the 2 subunits of LFA-1. TRM_{stem} cells also expressed markers of stem-like cells described in viral infections, including *IL7R*, *CD28*, and *CCR7*. Consistent with prolonged responses against specific tumor antigens, TRM_{exh} cells exhibited the highest clonality (Figures 4D and 4E). In these tumors, 57.7% of TRM-like clonotypes shared 998 TCRs with TRM_{stem} cells (Figures 4F, 4G, and S5K). Including TRM_{stem} clonotypes without a detectable differentiation trajectory in our analysis, 36.6% of TCRs in TRM-like cells (11,448 unique TRM-like clonotypes in 8 tumors) are represented in the TRM_{stem} compartment (Figures 4G and S5K). Given that only 40% of the non-redundant TCR repertoire is contained in TRM-like TILs (as opposed to 67% in recirculating lymphocytes; Table S2), clonotypes with a progenitor TRM_{stem} reservoir plus differentiated TRM-like cells only represent ~3% of TCRs (equates to 13.4% of $CD8^{+}$ TILs). Together, these results implied that only a narrow subset of recirculating TILs transition to acquire a TRM_{stem} reservoir, which can produce waves of $TRM_{eff} \rightarrow TRM_{prol} \rightarrow TRM_{exh,}$ T cells, and identifies clonotypes with clear signs of active tumor antigen recognition.

To confirm that these enriched clonotypes were indeed tumor reactive, we expressed 5 of these TCRs from 2 different tumors in TCR-β chain-negative Jurkat76 cells. As shown in Figure 5A, incubation with the autologous dissociated tumor elicited interleukin-2 (IL-2) production by TCR-transduced (but not control, mock-transduced) Jurkat76 cells, indicative of tumor antigen recognition, which represent truly tumor-reactive lymphocytes.

To verify the protective role of TRM_{stem} TILs in human ovarian cancer, we next performed multiplex immunofluorescence on 122 different annotated HGSOCs (Figure 5B). Supporting previous reports (Webb et al., 2014), high ratios of TRM-like versus recirculating $CD8^{+}$ TILs were associated with improved overall survival, both in total tumor and specifically in PCK^{+} tumor islets (Figures 5C and S6A). However, the improved survival associated with $CD3^{+}$ TILs was only significant for intra-epithelial lymphocytes (Figure S6A). Notably, TRM-like TILs were predominantly located inside tumor islets, while their recirculating counterparts were scattered throughout the stroma as well as tumor cells (Figure 5D). Tumor infiltration by $CD3^{+}CD8^{+}CD103^{low}$ $CD69^{+}$ TRM-like cells expressing the TRM_{stem} markers TCF1 was also strongly associated with superior outcome (Figure 5E). In contrast, the accumulation of $TCF1^{+}CD103^{-}CD8^{+}$ (stem-like recirculating) T cells (Figure 5F), or $TCF1^{+}CD103^{-}CD8^{+}CD69^{-}$ (resting recirculating) T cells (Figure 5G) was not. Similarly, the density of $TCF1^{-}CD103^{+}CD69^{+}CD8^{+}$ (differentiated TRM-like) TILs in histological sections without detectable TRM_{stem} cells (Figure 5H) was not significantly associated with outcome, although it had predictive value when TRM_{stem} cells were not segregated (Figure S6B).

Unexpectedly, we found that $CLEC9A^{+}$ dendritic cells preferentially cluster with recirculating TILs, compared to TRM-like cells (Figure S6C). Future studies should determine whether this illustrates a transient, recently activated phenotype (Duraiswamy et al., 2021; Menares et al., 2019).

Spatial analyses of interactions between different cell types showed a strong association between TRM_{stem} cells and other TRM-like cells, although TRM_{stem} cells also clustered with $CD69^{+}$ recirculating T cells (Figures 5I and S6D–S6F). Accordingly, 2-dimensional t-distributed stochastic neighbor embedding (2D t-SNE) rendering of all of the tumors analyzed showed distinct clusters of TRM_{stem} cells and more differentiated TRM-like cells, in addition to interactions between downstream TRM-like cells and recirculating T cells (Figure 5J). Together, these experiments confirmed the linear trajectory of differentiation of TRM-like cells and indicated that the association between TRM-like TILs and better outcomes depends on the density of TRM_{stem} cells.

Generating and maintaining a reservoir of protective tumor-reactive TRM_{stem} cells depends on the quality of T cell priming and persistence of cognate antigen at tumor beds

To understand what determines the generation of a TRM_{stem} reservoir by only some tumor-reactive T cells, we focused on the magnitude of antigen priming (Figure 6A). For adoptive transfer, *de novo* stimulation of $CD8^{+}$ OT-I cells using antigen-pulsed syngeneic dendritic cells generated $CD69^{+}CD103^{-}$ OT-I T cells (Figure S6G). As shown in Figure 6B, activating OVA-specific T cells *in vitro* with different doses of cognate (SIINFEKL) antigen did not affect their accumulation at OVA^{+} tumor beds, the subsequent density of tumor-reactive TRM-like cells, or the balance of $TRM_{stem}/TRM_{eff.}$ cells (Figure 6C). However, tumor antigen-specific T cells required activation by antigen-pulsed antigen-presenting cells (APCs) to accumulate at tumor beds, suggesting T cell

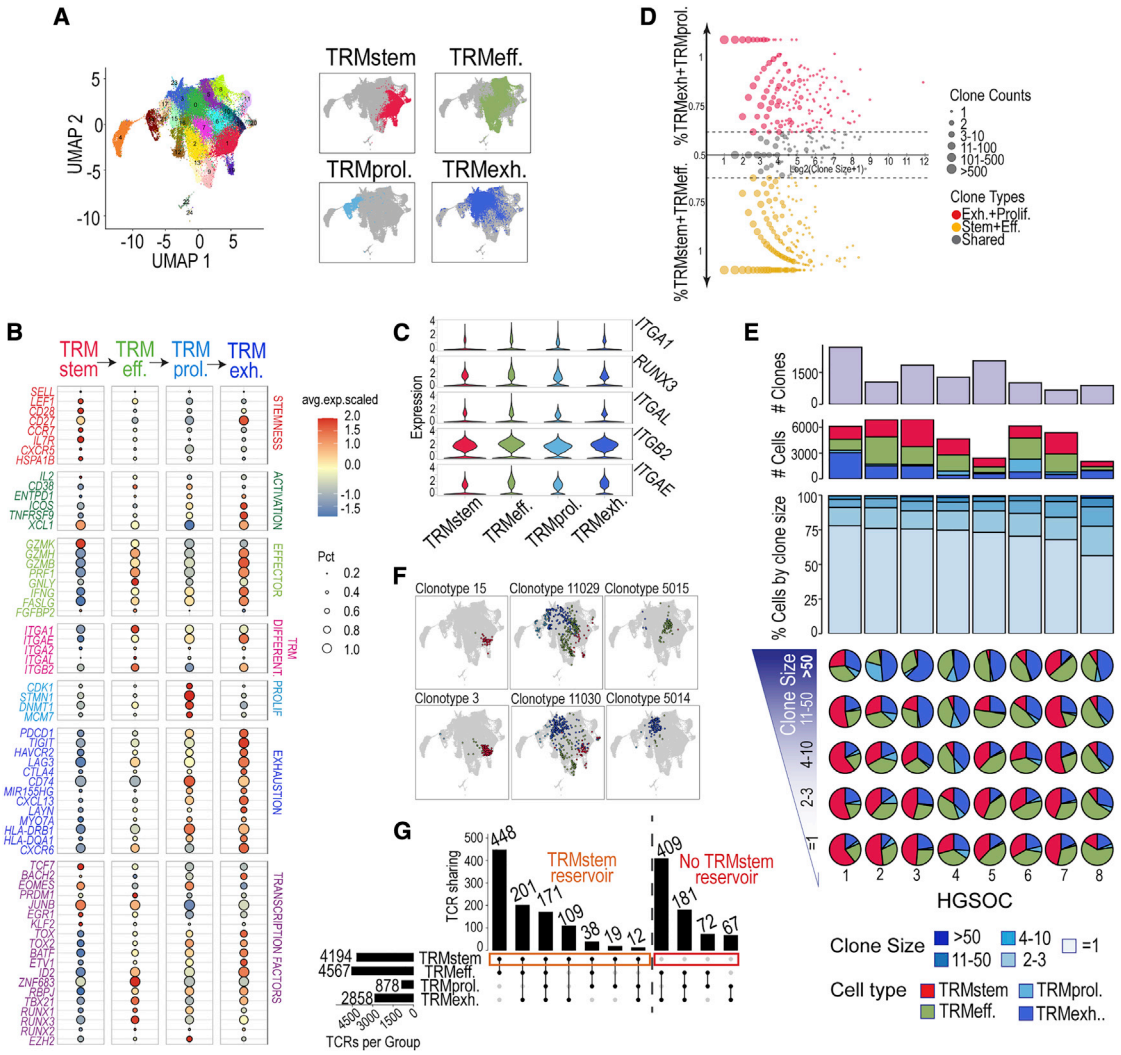

Figure 4. Clonal enrichment of TILs with TCRs shared by TRM_{stem} and downstream TRM-like phenotypes

(A) Left: UMAP of 60,010 TRM-like $CD8^+$ TILs sorted from 8 HGSOCs showing 25 clusters according to the gene expression. Right: Cells are colored by 4 major groups.

(B) Bubble plot of the relative expression emphasizing the same genes highlighted in Figure 3. The color of each dot presents the average expression from high (red) to low (blue). The size of each dot represents the percentage of positive cells for each gene.

(C) Violin plot showing the normalized gene expression of genes involved in TRM-like differentiation in the 4 major groups.

(D) TCR sharing between TRM_{stem}, TRM_{eff}, TRM_{prol}, and TRM_{exh}. Yellow dots represent clones dominated by TRM_{stem}/TRM_{eff} cells (>60%). Red dots represent clones dominated by TRM_{prol}/TRM_{exh} cells (>60%). Gray dots represent clones shared between TRM_{stem}/TRM_{eff} and TRM_{prol}/TRM_{exh} cells. The size of the dots represents the number of clones with the same number of cells. X axis denotes the log2-scale of cell count within each clone. TRM_{exh}/TRM_{prol} have more larger clones and thus higher clonality than other groups.

(E) Clonal composition of TRM-like $CD8^+$ TILs in the 8 HGSOCs. From top to bottom, the number of different clones per tumor, the number of TRM-like TILs with productive VDJ sequences colored by group, the distribution of the clones by size (color in the bars show = 1, 2–3, 4–10, 11–50, >50 cells), and the piecharts show the TRM-like group composition of clones stratified by size (color represents the TRM-like group) in each tumor.

(F) Clonotypes showing different trajectories. Each UMAP contain 1 unique clonotype and the cells belonging to the clonotype are colored by TRM-like groups. Left: Clonotypes only expressed in TRM_{stem}; center: clonotypes showing the full trajectory; and right: clonotypes that have lost the TRM_{stem} reservoir.

(G) TCR sharing between the TRM-like groups obtained by scVDJ profiling. The bar on the left shows the number of unique clonotypes in each group. The bar at the top panel shows the number of clonotypes shared by the groups.

See also Figure S5 and Table S4.

unresponsiveness after undergoing metabolic paralysis in the TME (Figure 6D) (Song et al., 2018).

To elucidate the role of antigen affinity in TRM_{stem} differentiation, we next compared phenotypic differences between OT-I T cells activated *in vitro* in response to the cognate antigen for the OT-1 TCR (SIINFEKL) versus low-affinity ligands Q4H7 (SIIQFEHL) and G4 (SIIGFEKL) (Mallaun et al., 2008). Activating with low-affinity SIIQFEHL or SIIGFEKL diminished the capacity of tumor-reactive OT-I cells to accumulate at tumor beds (Figure 6E) and to undergo TRM-like differentiation (Figure 6F),

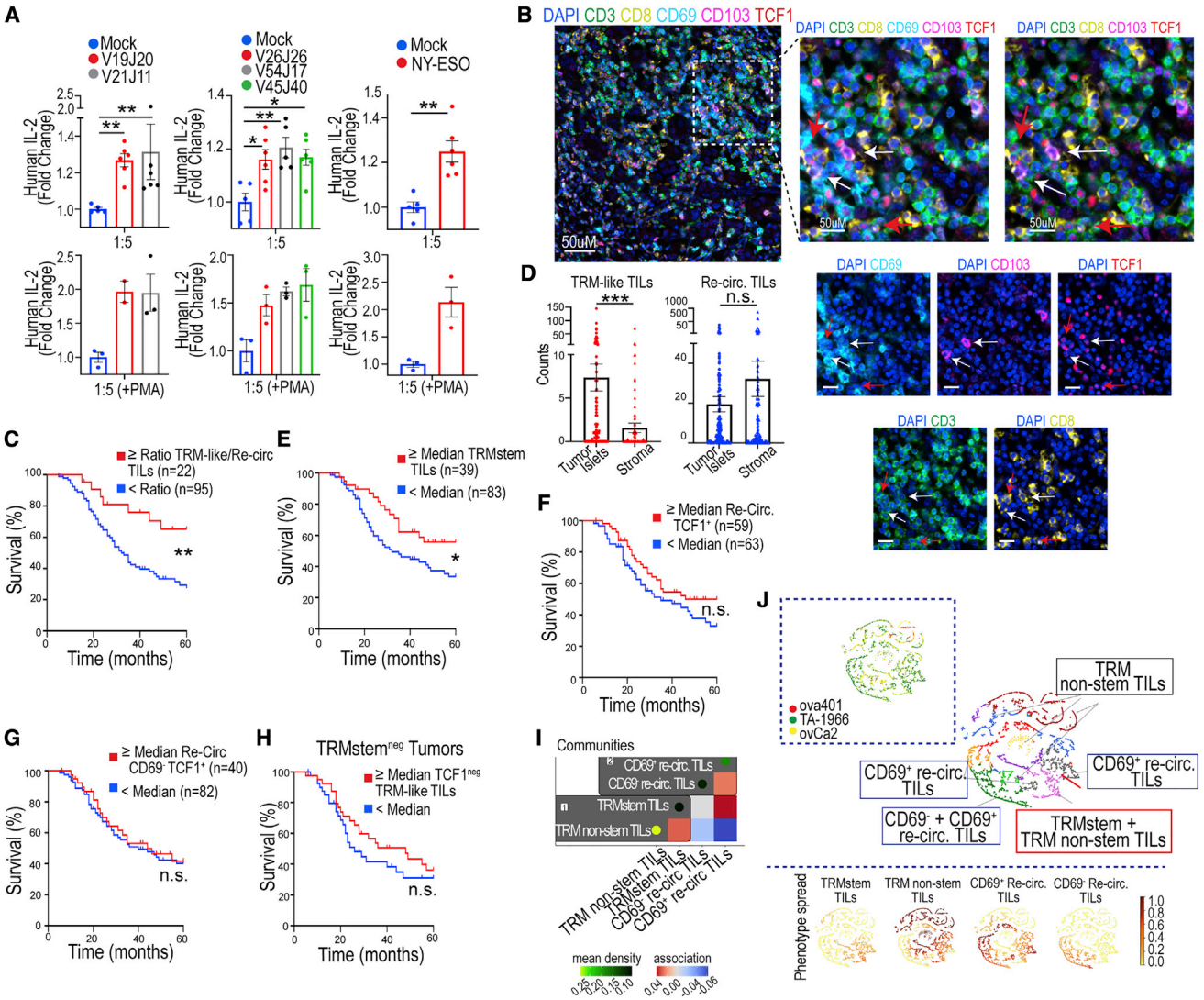

Figure 5. TRM_{stem} cell recognize specific tumor antigens and correlate with better survival

(A) Jurkat76 cells co-transduced with CD3 complex and 5 different TCRs identified from 2 different tumors or with CD3 complex and empty vector (mock) were co-cultured with the corresponding immortalized tumor cells (tumor-sorted $CD45^{-}EpCAM^{+}$ primary HGSOC cells) at a ratio of 1:5 (tumor:Jurkat). IL-2 levels in the supernatant were measured by ELISA after 48 h. Jurkat76 co-transduced with CD3 complex and NY-ESO-1-TCR were co-cultured with artificial APCs (aAPCs) (K32) expressing HLA:A2 and NY-ESO-1 peptide as a positive control (top). Representative from 2 independent experiments. Data show means with SEMs Statistical analysis was performed by unpaired t test non-parametric (Mann-Whitney test). *$p < 0.05$, **$p \leq 0.01$, ***$p \leq 0.001$. To increase IL-2 production by Jurkat76, PMA was added at 10 ng/mL to the co-culture (bottom).

(B) Representative images from tumor sections (n = 122) of multiplex immunohistochemistry of combined staining of CD3, CD8, CD69, CD103, TCF1, and DAPI (top left). Magnified images of the combined staining of the same colors (center) and without CD69 (right) indicating the presence of TRM_{stem} (white arrows) and $TCF1^{+}$ recirculating (red arrows) $CD8^{+}$ TILs. Images of single staining from each marker in the bottom. Scale bar, 50 μm.

(C) Overall survival associated with higher ratios of TRM-like/recirculating $CD8^{+}$ TILs in HGSOCs, as assessed by multiplex immunofluorescence.

(D) Distribution (in number of cell counts) of TRM-like ($CD3^{+}CD8^{+}CD69^{+}CD103^{+}$) and recirculating $CD8^{+}$ TILs ($CD3^{+}CD8^{+}CD103^{-}$) in tumor islets and stroma. Data show means with SEMs of 122 HGSOCs. Statistical analysis performed by paired t test non-parametric (Wilcoxon test). *$p < 0.05$, **$p \leq 0.01$, ***$p \leq 0.001$.

(E) Survival outcome associated with the presence of TRM_{stem} ($CD3^{+}CD8^{+}CD69^{+}CD103^{+}TCF1^{+}$) in 122 HGSOCs from 3 independent tumor tissue microarrays (TMAs).

(F) Higher density of stem-like recirculating ($TCF1^{+}CD103^{-}CD8^{+}$) or (G) resting recirculating TILs ($TCF1^{+}CD103^{-}CD8^{+}CD69^{-}$) is not associated with better outcomes.

(H) In sections in which TRM_{stem} were not detected, the presence of differentiated TRMs-like ($CD69^{+}CD103^{+}TCF1^{neg}$) was not significantly associated with improved survival. *$p \leq 0.05$, **$p \leq 0.01$, 2-sided log rank (Mantel-Cox) test.

(I) A spatial interaction network was fitted to the spatial distribution of cells, which was subsequently simplified via community detection. Negative values (blue) indicate spatial repulsion, while positive values (red) indicate spatial attraction. Gray boxes contain cell types found within the same community.

(J) Left box: t-SNE rendering showing distribution of the 3 TMAs used in this analysis. Top: 2D t-SNE rendering showing distinct clusters of TRM-like cells and recirculating T cells where TRM_{stem} clusters exclusively with other TRM-like cells, while other populations exist as distinct clusters of their own. Bottom: t-SNE

(legend continued on next page)

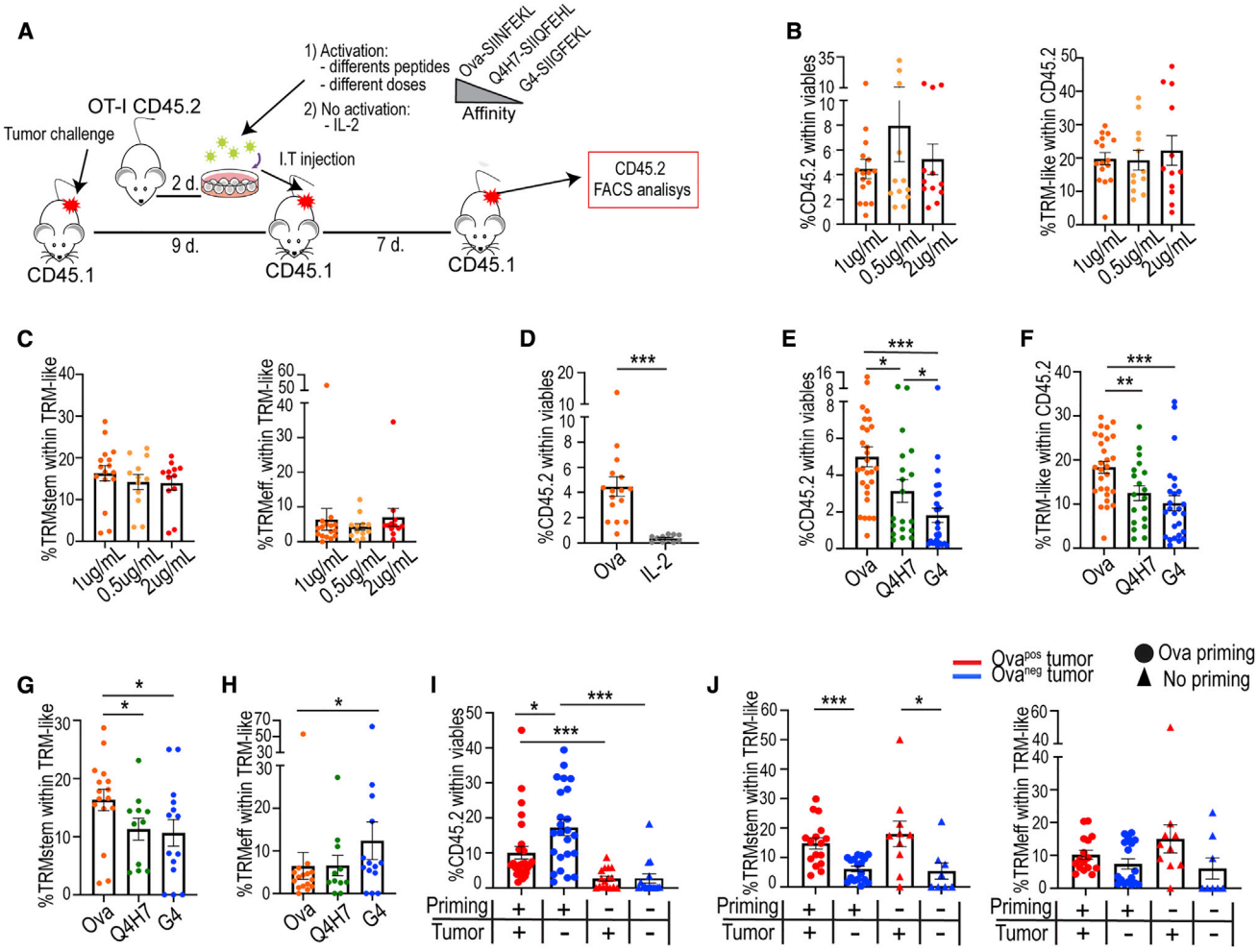

Figure 6. Strong priming and persistence of the antigen at tumor beds are required for the generation and maintenance of TRM_{stem} $CD8^+$ TILs

(A) Experimental setting.

(B) FACS analysis of $CD45.2^+$ and TRM-like $CD8^+$ TILs from OVA^{low}-UPK10 tumors 7 days after intratumoral injection with purified $CD8^+$ OT-I T cells, activated for 2 days with SIINFEKL at 1/0.5/2 μg/mL.

(C) Percentage of TRM_{stem} ($CD45.2^+CD3^+CD8^+CD69^+CD103^+IL7R^+TCF1^+$) or $TRM_{eff.}$ ($CD45.2^+CD3^+CD8^+CD69^+CD103^+MHC\text{-}II^+CXCR6^+$) within TRM-like $CD8^+$ OT-I TILs in OVA^{low}-UPK10 tumors, 7 days after intratumoral injection with purified, SIINFEKL-activated $CD8^+$ OT-I T cells (1/0.5/2 μg/mL).

(D) Proportion of intratumoral transferred OT-I T cells, activated 2 days before with SIINFEKL versus incubated with control IL-2.

(E–H) Quantification of CD45.2 (E); (F) TRM-like OVA-specific $CD8^+$ TILs; (G) TRM_{stem}; and (H) TRM_{eff}, within TRM-like TILs from OVA^{low}-UPK10 tumors, after activation with SIINFEKL or lower affinity peptides, Q4H7 (SIIQFEHL) and G4 (SIIGFEKL).

(I and J) FACS analysis of $CD45.2^+$ (I) and J) TRM_{stem} and TRM_{eff} cells within OT-I TRM-like TILs sorted from UPK10 tumors transduced with OVA^{low} (red) or empty vector (mock, blue). SIINFEKL-activated OT-I cells and OT-I cells maintained with IL-2 (control) are shown. Pooled from 3 independent experiments.

For (E, F, and I), pooled from 5 independent experiments. Data are represented as means with SEMs Each dot represents 1 mouse. Unpaired t test non-parametric (Mann-Whitney test). *$p < 0.05$, **$p \leq 0.01$, ***$p \leq 0.001$.

See also Figure S6.

compared to SIINFEKL activation, in an affinity-dependent manner. However, OT-I cells activated *in vitro* with the different peptides, maintained in culture for longer periods, did not become TRM-like cells (Figure S6H). Furthermore, fewer TRM-like TILs activated with low-affinity Q4H7 or G4 retain TCF1 expression, which is indicative of defective TRM_{stem} formation (Figure 6G). In contrast, higher proportions of $TRM_{eff.}$ TILs were found with suboptimal priming (Figure 6H).

Besides the quality of priming, antigen persistence at tumor beds was also required for the optimal formation of a TRM_{stem} pool. Thus, although optimally *in vitro*-activated OT-I cells effectively accumulated at OVA^- tumors (Figure 6I), including as

image showing the distribution of the 4 phenotypes, $TRM_{non\text{-}stem}$ ($CD3^+CD8^+CD69^+CD103^+TCF1^-$), TRM_{stem} ($CD3^+CD8^+CD69^+CD103^+TCF1^+$), $CD69^+$ re-circulating ($CD3^+CD8^+CD69^+CD103^-$), and $CD69^-$ recirculating ($CD3^+CD8^+CD69^-CD103^-$) TILs. The color bar from yellow to red indicates the distribution depth, with red depicting the highest distribution of a particular phenotype.

See also Figure S6.

TRM-like cells (Figures 2H and S1K), significantly lower TRM_{stem}/TRM_{eff} ratios were identified in the absence of cognate antigen (Figure 6J). Taken together, these results suggested that the quality of T cell priming and persistence of tumor antigen in the TME, are required for the formation and maintenance of a TRM_{stem} cell pool with hybrid features of stemness and tissue residency, which generates waves of TRM-like cells that, through the active recognition of tumor antigen, progressively reach exhaustion.

DISCUSSION

Here, we reported that clonotypes showing obvious features of active recognition of ovarian cancer antigen represent 3% of total TCRs in $CD8^+$ T cells at ovarian cancer beds (285 of 9,422 TCRs in our analyses). These sequences could be identified based on their shared expression between TRM_{stem} and other differentiated TRM-like cells. Supporting reactivity against contemporarily expressed tumor antigens, these clonotypes were (1) clonally enriched, (2) exhibited a proliferative signature, and 3) expressed markers of effector activity. In addition, the prognostic value of $CD8^+$ TILs was dependent on TRM_{stem} cell infiltration, while maintaining a TRM_{stem} phenotype required the active expression of tumor antigen. Accordingly, 5 different TCRs shared between TRM_{stem} cells and other downstream TRM-like subsets recognized autologous tumor. Therefore, beyond prognostic associations for TILs and despite the paucity of tumor-reactive T cells and poor response to current immunotherapies, human ovarian cancer is indeed a T cell immunogenic disease.

Based on the consistent evolution of transcriptional and chromatin structure patterns in TILs sharing the same TCR, TRM_{stem} cells arose from distinct $CD103^-$ T cells, and progressively differentiated into effector, proliferating/pre-exhausted, and truly exhausted TRM-like cells. However, 77% of TRM_{stem} clones lacked a detectable clonally expanded TRM_{eff} or TRM_{exh} counterpart. Some could represent T cells responding to recently expressed neoantigens (i.e., arising from new mutations), which are in the process of generating new waves of differentiated TRM-like cells. Alternatively, there may be differentiated TRM-like cells in other areas of the tumor or in frequencies that cannot be detected through single-cell analyses, or the antigens that they recognize could be disappearing from that tumor location.

Our results provided multiple insights into the immunobiology of human ovarian cancer, giving new opportunities to improve the immunotherapy that has not been effective for most ovarian cancer patients for several reasons such as the presence of other dominant immunosuppressive signals that prevent T cell reactivation, metabolic restrictions of the tumor ascites and the peritoneal cavity, and stronger accumulation of immunosuppressive myeloid cells than in other diseases. First, we provided evidence that trogocytic (antigen-specific) T cells can be identified at tumor beds. It is therefore tempting to speculate that personalized therapies using selected TIL expansion, or T cells transduced with specific TCRs, could be implemented in a personalized manner without knowing the precise target. This could include a range of clonotypes that overcome inter-metastatic heterogeneity in terms of antigenic drivers. Second, we found that TRM-like $CD8^+$ TILs and their recirculating counterparts represent very distinct compartments in terms of phenotype and antigen recognition. The narrow set of common TCRs clones was randomly distributed among different TRM-like clusters, strongly suggesting that most recirculating TILs (~40% of $CD8^+$ TILs and 67% of $CD8^+$ T cell clonotypes) are primarily bystanders in the TME. Third, we identify pivotal TRM_{stem} cells as an intermediate cell type sharing the determinants of both stemness and tissue residency. Previous studies identified TRM-like cells and stem-like TILs in cancer as distinct cell types, although the former can arise from the latter (Siddiqui et al., 2019). Our results supported recent studies from suggesting that TRM-like precursors eventually turn into terminally differentiated cells (Gueguen et al., 2021). Interestingly, the effectiveness of immune checkpoint blockade has been attributed to the proliferation of a stem-like TIL subset that is different from TRM cells in some studies (Siddiqui et al., 2019), while others found that it depends on TRM cells (Ganesan et al., 2017). Considering that several factors influence survival, such as the variability of antigenic drivers between patients and the heterogeneity of expression of the chemokines that recruit T cells, our data supported that, at least in ovarian cancer, the density of a subset of $CD103^{low}$ TRM-like lymphocytes that retains features of stemness while differentiating into TRM-like cells, but not $CD103^-TCF1^+CD8^+$ TILs, predicts ovarian cancer survival. However, 9.2% of stem-like recirculating T cell clones were shared by TRM_{stem} clones. They likely represented recently primed tumor-reactive T cells transitioning to acquire attributes of tissue-resident differentiation before becoming TRM_{stem} TILs. Because only 24% of TRM_{stem} clones shared TCRs with TILs showing features of antigen recognition (i.e., intratumoral clonal expansion), it seems plausible that the active recognition of tumor antigen in untreated ovarian cancers depends on ~3% of $CD8^+$ clones at tumor beds.

Another important aspect of our study was the demonstration that TRM-like differentiation equips tumor-reactive T cells to exert superior immune pressure at tumor beds, compared to clonal TILs that remain as recirculating cells. Interestingly, TRM-like differentiation did not require re-encounter with an antigen in the TME, further suggesting that most TILs are either bystander cells or TRM-like cells that remain at tumor beds after tumor antigen clearance through immuno-editing.

In summary, our results, supported by bioinformatical analysis, point to a model in which a small subset of recently primed recirculating T cells undergo TRM differentiation. Depending on the intensity of activation and the myeloid microenvironment, some lymphocytes turn into TRM_{stem} TILs, with the capacity to generate new waves of effector lymphocytes and exert effective immune pressure, while others will directly advance to exhaustion after repeated exposure to antigens, without a TRM_{stem} reservoir.

STAR★METHODS

Detailed methods are provided in the online version of this paper and include the following:

- KEY RESOURCES TABLE
- RESOURCE AVAILABILITY
  - Lead contact
  - Materials availability
  - Data and code availability
- EXPERIMENTAL MODEL AND SUBJECT DETAILS
  - Human samples

SUPPLEMENTAL INFORMATION

Supplemental information can be found online at https://doi.org/10.1016/j.ccell.2022.03.008.

ACKNOWLEDGMENTS

Support for Shared Resources was provided by Cancer Center Support Grant (CCSG) CA076292 to the H. Lee Moffitt Cancer Center and by CCSG CA010815 to The Wistar Institute. We are particularly grateful to the Bioinformatics, Genomics, Flow Cytometry (an NCI-designated Comprehensive Cancer Center, P30-CA076292), Microscopy, and Digital Pathology Shared Facilities at Moffitt for outstanding technical support. Special thanks to Neelkamal Chaudhary (Flow Cytometry core), Johnson Joseph (Analytic Microscopy core), Jonathan Nguyen (CLIA imaging lab), and Chaomei Zhang (Molecular Genomics core) for commendable support. This study was supported by R01CA157664, R01CA124515, R01CA178687, R01CA211913, and U01CA232758 to J.R.C.-G., and R01CA184185 and RO1CA262121 to P.C.R. K.K.P. was supported by T32CA009140 and The American Cancer Society Postdoctoral Fellowship. S.B. was supported by K99CA266947-01 and JSRP Moffitt Cancer Center.

AUTHOR CONTRIBUTIONS

C.M.A., X.Y., and J.R.C.-G. conceptualized the study, developed the methodology, and performed the visualization. C.M.A., K.H., S.B., R.C., A.M., J.M., K.S., and T.L.C. performed the study investigation. C.M.A., X.Y., C.D.G., and S.P. performed the formal analysis. K.K.P., M.H.H., A.R.A., R.M.W., P.C.R., and J.R.C.-G. obtained the resources. C.M.A. and J.R.C.-G. performed the validation and wrote the original draft. All of the authors reviewed and edited the manuscript. J.R.C.-G. obtained the funding and supervised the study.

DECLARATION OF INTERESTS

J.R.C.-G. has stock options with Compass Therapeutics, Anixa Biosciences, and Alloy Therapeutics; receives honorarium from Anixa Biosciences, Alloy Therapeutics, and Leidos; and has sponsored research with Anixa Biosciences (all outside the submitted work). B.A.P. has served on the Advisory Board of AstraZeneca and has research support from BMS. J.R.C.-G. is currently an employee of STEMCELL Technologies (all work outside the submitted work). R.M.W. reports grants and personal fees from Merck, personal fees from Tesaro/GSK, personal fees from Genentech, personal fees from Legend Biotech, personal fees from AbbVie, personal fees from Astrazeneca, grants and stock from Ovation Diagnostics, personal fees from Clovis Oncology, and personal fees from Regeneron (all outside the submitted work).

Received: October 26, 2021
Revised: February 6, 2022
Accepted: March 23, 2022
Published: April 14, 2022

REFERENCES

Aibar, S., González-Blas, C.B., Moerman, T., Huynh-Thu, V.A., Imrichova, H., Hulselmans, G., Rambow, F., Marine, J.-C., Geurts, P., Aerts, J., et al. (2017). SCENIC: single-cell regulatory network inference and clustering. Nat. Methods *14*, 1083–1086.

Amsen, D., van Gisbergen, K., Hombrink, P., and van Lier, R.A.W. (2018). Tissue-resident memory T cells at the center of immunity to solid tumors. Nat. Immunol. *19*, 538–546.

Ashburner, M., Ball, C.A., Blake, J.A., Botstein, D., Butler, H., Cherry, J.M., Davis, A.P., Dolinski, K., Dwight, S.S., Eppig, J.T., et al. (2000). Gene ontology: tool for the unification of biology. The Gene Ontology Consortium. Nat. Genet. *25*, 25–29.

Baddeley, A., and Turner, R. (2005). Spatstat: an R package for analyzing spatial point patterns. J. Stat. Softw. *12*, 1–42.

Baddeley, A., and Turner, R. (2006). Modelling spatial point patterns in R. In Case Studies in Spatial Point Process Modeling, A. Baddeley, P. Gregori, J. Mateu, R. Stoica, and D. Stoyan, eds. (Springer New York), pp. 23–74.

Baumeister, S.H., Freeman, G.J., Dranoff, G., and Sharpe, A.H. (2016). Coinhibitory pathways in immunotherapy for cancer. Annu. Rev. Immunol. *34*, 539–573.

Blank, C.U., Haining, W.N., Held, W., Hogan, P.G., Kallies, A., Lugli, E., Lynn, R.C., Philip, M., Rao, A., Restifo, N.P., et al. (2019). Defining 'T cell exhaustion'. Nat. Rev. Immunol. *19*, 665–674.

Blondel, V.D., Guillaume, J.-L., Lambiotte, R., and Lefebvre, E. (2008). Fast unfolding of communities in large networks. J. Stat. Mech. Theor. Exp. *2008*, P10008.

Bourdely, P., Anselmi, G., Vaivode, K., Ramos, R.N., Missolo-Koussou, Y., Hidalgo, S., Tosselo, J., Nunez, N., Richer, W., Vincent-Salomon, A., et al. (2020). Transcriptional and functional analysis of CD1c(+) human dendritic cells identifies a CD163(+) subset priming CD8(+)CD103(+) T cells. Immunity *53*, 335–352.e8.

Cao, Y., Trillo-Tinoco, J., Sierra, R.A., Anadon, C., Dai, W., Mohamed, E., Cen, L., Costich, T.L., Magliocco, A., Marchion, D., et al. (2019). ER stress-induced mediator C/EBP homologous protein thwarts effector T cell activity in tumors through T-bet repression. Nat. Commun. *10*, 1280.

Conway, J.R., Lex, A., and Gehlenborg, N. (2017). UpSetR: an R package for the visualization of intersecting sets and their properties. Bioinformatics *33*, 2938–2940.

Corgnac, S., Boutet, M., Kfoury, M., Naltet, C., and Mami-Chouaib, F. (2018). The emerging role of CD8(+) tissue resident memory T (TRM) cells in antitumor

immunity: a unique functional contribution of the CD103 integrin. Front. Immunol. *9*, 1904.

Curiel, T.J., Wei, S., Dong, H., Alvarez, X., Cheng, P., Mottram, P., Krzysiek, R., Knutson, K.L., Daniel, B., Zimmermann, M.C., et al. (2003). Blockade of B7-H1 improves myeloid dendritic cell-mediated antitumor immunity. Nat. Med. *9*, 562–567.

Dobin, A., Davis, C.A., Schlesinger, F., Drenkow, J., Zaleski, C., Jha, S., Batut, P., Chaisson, M., and Gingeras, T.R. (2013). STAR: ultrafast universal RNA-seq aligner. Bioinformatics *29*, 15–21.

Dumauthioz, N., Labiano, S., and Romero, P. (2018). Tumor resident memory T cells: new players in immune surveillance and therapy. Front. Immunol. *9*, 2076.

Duraiswamy, J., Turrini, R., Minasyan, A., Barras, D., Crespo, I., Grimm, A.J., Casado, J., Genolet, R., Benedetti, F., Wicky, A., et al. (2021). Myeloid antigen-presenting cell niches sustain antitumor T cells and license PD-1 blockade via CD28 costimulation. Cancer Cell *39*, 1623–1642.e20.

FitzPatrick, M.E.B., Provine, N.M., Garner, L.C., Powell, K., Amini, A., Irwin, S.L., Ferry, H., Ambrose, T., Friend, P., Vrakas, G., et al. (2021). Human intestinal tissue-resident memory T cells comprise transcriptionally and functionally distinct subsets. Cell Rep. *34*, 108661.

Ganesan, A.P., Clarke, J., Wood, O., Garrido-Martin, E.M., Chee, S.J., Mellows, T., Samaniego-Castruita, D., Singh, D., Seumois, G., Alzetani, A., et al. (2017). Tissue-resident memory features are linked to the magnitude of cytotoxic T cell responses in human lung cancer. Nat. Immunol. *18*, 940–950.

Godec, J., Tan, Y., Liberzon, A., Tamayo, P., Bhattacharya, S., Butte, A.J., Mesirov, J.P., and Haining, W.N. (2016). Compendium of immune signatures identifies conserved and species-specific biology in response to inflammation. Immunity *44*, 194–206.

Granja, J.M., Klemm, S., McGinnis, L.M., Kathiria, A.S., Mezger, A., Corces, M.R., Parks, B., Gars, E., Liedtke, M., Zheng, G.X.Y., et al. (2019). Single-cell multiomic analysis identifies regulatory programs in mixed-phenotype acute leukemia. Nat. Biotechnol. *37*, 1458–1465.

Gu, Z., Eils, R., and Schlesner, M. (2016). Complex heatmaps reveal patterns and correlations in multidimensional genomic data. Bioinformatics *32*, 2847–2849.

Gueguen, P., Metoikidou, C., Dupic, T., Lawand, M., Goudot, C., Baulande, S., Lameiras, S., Lantz, O., Girard, N., Seguin-Givelet, A., et al. (2021). Contribution of resident and circulating precursors to tumor-infiltrating CD8(+) T cell populations in lung cancer. Sci. Immunol. *6*, eabd5778.

Harjes, U. (2020). The source within - intratumoural stem-like T cells give rise to differentiated T cells. Nat. Rev. Cancer *20*, 140.

Hartana, C.A., Ahlen Bergman, E., Broome, A., Berglund, S., Johansson, M., Alamdari, F., Jakubczyk, T., Huge, Y., Aljabery, F., Palmqvist, K., et al. (2018). Tissue-resident memory T cells are epigenetically cytotoxic with signs of exhaustion in human urinary bladder cancer. Clin. Exp. Immunol. *194*, 39–53.

Hombrink, P., Helbig, C., Backer, R.A., Piet, B., Oja, A.E., Stark, R., Brasser, G., Jongejan, A., Jonkers, R.E., Nota, B., et al. (2017). Erratum: programs for the persistence, vigilance and control of human CD8(+) lung-resident memory T cells. Nat. Immunol. *18*, 246.

Hudson, W.H., Gensheimer, J., Hashimoto, M., Wieland, A., Valanparambil, R.M., Li, P., Lin, J.X., Konieczny, B.T., Im, S.J., Freeman, G.J., et al. (2019). Proliferating transitory T cells with an effector-like transcriptional signature emerge from PD-1(+) stem-like CD8(+) T cells during chronic infection. Immunity *51*, 1043–1058.e4.

Hunter, J.D. (2007). Matplotlib: a 2D graphics environment. Comput. Sci. Eng. *9*, 90–95.

Jadhav, R.R., Im, S.J., Hu, B., Hashimoto, M., Li, P., Lin, J.X., Leonard, W.J., Greenleaf, W.J., Ahmed, R., and Goronzy, J.J. (2019). Epigenetic signature of PD-1+ TCF1+ CD8 T cells that act as resource cells during chronic viral infection and respond to PD-1 blockade. Proc. Natl. Acad. Sci. U S A *116*, 14113–14118.

Jansen, C.S., Prokhnevska, N., Master, V.A., Sanda, M.G., Carlisle, J.W., Bilen, M.A., Cardenas, M., Wilkinson, S., Lake, R., Sowalsky, A.G., et al. (2019). An intra-tumoral niche maintains and differentiates stem-like CD8 T cells. Nature *576*, 465–470.

Joly, E., and Hudrisier, D. (2003). What is trogocytosis and what is its purpose? Nat. Immunol. *4*, 815.

Khan, O., Giles, J.R., McDonald, S., Manne, S., Ngiow, S.F., Patel, K.P., Werner, M.T., Huang, A.C., Alexander, K.A., Wu, J.E., et al. (2019). TOX transcriptionally and epigenetically programs CD8(+) T cell exhaustion. Nature *571*, 211–218.

Kobak, D., and Berens, P. (2019). The art of using t-SNE for single-cell transcriptomics. Nat. Commun. *10*, 5416.

Korotkevich, G., Sukhov, V., Budin, N., Shpak, B., Artyomov, M.N., and Sergushichev, A. (2021). Fast gene set enrichment analysis. Preprint at bioRxiv. https://doi.org/10.1101/060012.

Korsunsky, I., Millard, N., Fan, J., Slowikowski, K., Zhang, F., Wei, K., Baglaenko, Y., Brenner, M., Loh, P.-r., and Raychaudhuri, S. (2019). Fast, sensitive and accurate integration of single-cell data with Harmony. Nat. Methods *16*, 1289–1296.

Kumar, B.V., Ma, W., Miron, M., Granot, T., Guyer, R.S., Carpenter, D.J., Senda, T., Sun, X., Ho, S.H., Lerner, H., et al. (2017). Human tissue-resident memory T cells are defined by core transcriptional and functional signatures in lymphoid and mucosal sites. Cell Rep. *20*, 2921–2934.

Liao, Y., Smyth, G.K., and Shi, W. (2013). featureCounts: an efficient general purpose program for assigning sequence reads to genomic features. Bioinformatics *30*, 923–930.

Liberzon, A., Subramanian, A., Pinchback, R., Thorvaldsdóttir, H., Tamayo, P., and Mesirov, J.P. (2011). Molecular signatures database (MSigDB) 3.0. Bioinformatics *27*, 1739–1740.

Liberzon, A., Birger, C., Thorvaldsdóttir, H., Ghandi, M., Mesirov, J.P., and Tamayo, P. (2015). The Molecular Signatures Database (MSigDB) hallmark gene set collection. Cell Syst. *1*, 417–425.

Mackay, L.K., Rahimpour, A., Ma, J.Z., Collins, N., Stock, A.T., Hafon, M.L., Vega-Ramos, J., Lauzurica, P., Mueller, S.N., Stefanovic, T., et al. (2013). The developmental pathway for CD103(+)CD8+ tissue-resident memory T cells of skin. Nat. Immunol. *14*, 1294–1301.

Mackay, L.K., Minnich, M., Kragten, N.A., Liao, Y., Nota, B., Seillet, C., Zaid, A., Man, K., Preston, S., Freestone, D., et al. (2016). Hobit and Blimp1 instruct a universal transcriptional program of tissue residency in lymphocytes. Science *352*, 459–463.

Malik, B.T., Byrne, K.T., Vella, J.L., Zhang, P., Shabaneh, T.B., Steinberg, S.M., Molodtsov, A.K., Bowers, J.S., Angeles, C.V., Paulos, C.M., et al. (2017). Resident memory T cells in the skin mediate durable immunity to melanoma. Sci. Immunol. *2*, eaam6346.

Mallaun, M., Naeher, D., Daniels, M.A., Yachi, P.P., Hausmann, B., Luescher, I.F., Gascoigne, N.R., and Palmer, E. (2008). The T cell receptor's alpha-chain connecting peptide motif promotes close approximation of the CD8 coreceptor allowing efficient signal initiation. J. Immunol. *180*, 8211–8221.

Martin, M. (2011). Cutadapt removes adapter sequences from high-throughput sequencing reads. EMBnet J. *17*, 3.

Masopust, D., and Soerens, A.G. (2019). Tissue-resident T cells and other resident leukocytes. Annu. Rev. Immunol. *37*, 521–546.

Menares, E., Galvez-Cancino, F., Caceres-Morgado, P., Ghorani, E., Lopez, E., Diaz, X., Saavedra-Almarza, J., Figueroa, D.A., Roa, E., Quezada, S.A., and Lladser, A. (2019). Tissue-resident memory CD8(+) T cells amplify anti-tumor immunity by triggering antigen spreading through dendritic cells. Nat. Commun. *10*, 4401.

Milner, J.J., Toma, C., Yu, B., Zhang, K., Omilusik, K., Phan, A.T., Wang, D., Getzler, A.J., Nguyen, T., Crotty, S., et al. (2017). Runx3 programs CD8(+) T cell residency in non-lymphoid tissues and tumours. Nature *552*, 253–257.

Molodtsov, A., and Turk, M.J. (2018). Tissue resident CD8 memory T cell responses in cancer and autoimmunity. Front. Immunol. *9*, 2810.

Mucha, P.J., Richardson, T., Macon, K., Porter, M.A., and Onnela, J.P. (2010). Community structure in time-dependent, multiscale, and multiplex networks. Science *328*, 876–878.

Mueller, S.N., and Mackay, L.K. (2016). Tissue-resident memory T cells: local specialists in immune defence. Nat. Rev. Immunol. *16*, 79–89.

Oja, A.E., Piet, B., Helbig, C., Stark, R., van der Zwan, D., Blaauwgeers, H., Remmerswaal, E.B.M., Amsen, D., Jonkers, R.E., Moerland, P.D., et al. (2018). Trigger-happy resident memory CD4(+) T cells inhabit the human lungs. Mucosal Immunol. *11*, 654–667.

Pan, Y., Tian, T., Park, C.O., Lofftus, S.Y., Mei, S., Liu, X., Luo, C., O'Malley, J.T., Gehad, A., Teague, J.E., et al. (2017). Survival of tissue-resident memory T cells requires exogenous lipid uptake and metabolism. Nature *543*, 252–256.

Parga-Vidal, L., Behr, F.M., Kragten, N.A.M., Nota, B., Wesselink, T.H., Kavazovic, I., Covill, L.E., Schuller, M.B.P., Bryceson, Y.T., Wensveen, F.M., et al. (2021). Hobit identifies tissue-resident memory T cell precursors that are regulated by Eomes. Sci. Immunol. *6*, eabg3533.

Park, S.L., Gebhardt, T., and Mackay, L.K. (2019). Tissue-resident memory T cells in cancer immunosurveillance. Trends Immunol. *40*, 735–747.

Pauken, K.E., Sammons, M.A., Odorizzi, P.M., Manne, S., Godec, J., Khan, O., Drake, A.M., Chen, Z., Sen, D.R., Kurachi, M., et al. (2016). Epigenetic stability of exhausted T cells limits durability of reinvigoration by PD-1 blockade. Science *354*, 1160–1165.

Pedregosa, F., Varoquaux, G., Gramfort, A., Michel, V., Thirion, B., Grisel, O., Blondel, M., Prettenhofer, P., Weiss, R., Dubourg, V., et al. (2011). Scikit-learn: machine learning in Python. J. Mach. Learn. Res. *12*, 2825–2830.

Pliner, H.A., Packer, J.S., McFaline-Figueroa, J.L., Cusanovich, D.A., Daza, R.M., Aghamirzaie, D., Srivatsan, S., Qiu, X., Jackson, D., Minkina, A., et al. (2018). Cicero predicts cis-regulatory DNA interactions from single-cell chromatin accessibility data. Mol. Cell *71*, 858–871.e8.

R Core Team (2019). R: A Language and Environment for Statistical Computing (R Foundation for Statistical Computing).

Rempala, G.A., and Seweryn, M. (2013). Methods for diversity and overlap analysis in T-cell receptor populations. J. Math. Biol. *67*, 1339–1368.

Rutkowski, M.R., Stephen, T.L., Svoronos, N., Allegrezza, M.J., Tesone, A.J., Perales-Puchalt, A., Brencicova, E., Escovar-Fadul, X., Nguyen, J.M., Cadungog, M.G., et al. (2015). Microbially driven TLR5-dependent signaling governs distal malignant progression through tumor-promoting inflammation. Cancer Cell *27*, 27–40.

Savas, P., Virassamy, B., Ye, C., Salim, A., Mintoff, C.P., Caramia, F., Salgado, R., Byrne, D.J., Teo, Z.L., Dushyanthen, S., et al. (2018). Single-cell profiling of breast cancer T cells reveals a tissue-resident memory subset associated with improved prognosis. Nat. Med. *24*, 986–993.

Scarlett, U.K., Rutkowski, M.R., Rauwerdink, A.M., Fields, J., Escovar-Fadul, X., Baird, J., Cubillos-Ruiz, J.R., Jacobs, A.C., Gonzalez, J.L., Weaver, J., et al. (2012). Ovarian cancer progression is controlled by phenotypic changes in dendritic cells. J. Exp. Med. *209*, 495–506.

Schurch, C.M., Bhate, S.S., Barlow, G.L., Phillips, D.J., Noti, L., Zlobec, I., Chu, P., Black, S., Demeter, J., McIlwain, D.R., et al. (2020). Coordinated cellular neighborhoods orchestrate antitumoral immunity at the colorectal cancer invasive. Front. Cell *182*, 1341–1359.e19.

Siddiqui, I., Schaeuble, K., Chennupati, V., Fuertes Marraco, S.A., Calderon-Copete, S., Pais Ferreira, D., Carmona, S.J., Scarpellino, L., Gfeller, D., Pradervand, S., et al. (2019). Intratumoral tcf1(+)PD-1(+)CD8(+) T cells with stem-like properties promote tumor control in response to vaccination and checkpoint blockade immunotherapy. Immunity *50*, 195–211.e10.

Song, M., Sandoval, T.A., Chae, C.S., Chopra, S., Tan, C., Rutkowski, M.R., Raundhal, M., Chaurio, R.A., Payne, K.K., Konrad, C., et al. (2018). IRE1alpha-XBP1 controls T cell function in ovarian cancer by regulating mitochondrial activity. Nature *562*, 423–428.

Stuart, T., Butler, A., Hoffman, P., Hafemeister, C., Papalexi, E., Mauck, W.M., 3rd, Hao, Y., Stoeckius, M., Smibert, P., and Satija, R. (2019). Comprehensive integration of single-cell data. Cell *177*, 1888–1902.e21.

Stuart, T., Srivastava, A., Lareau, C., and Satija, R. (2020). Multimodal single-cell chromatin analysis with Signac. Preprint at bioRxiv. https://doi.org/10.1101/2020.11.09.373613.

Subramanian, A., Tamayo, P., Mootha, V.K., Mukherjee, S., Ebert, B.L., Gillette, M.A., Paulovich, A., Pomeroy, S.L., Golub, T.R., Lander, E.S., and Mesirov, J.P. (2005). Gene set enrichment analysis: a knowledge-based approach for interpreting genome-wide expression profiles. Proc. Natl. Acad. Sci. U S A *102*, 15545–15550.

Szabo, P.A., Levitin, H.M., Miron, M., Snyder, M.E., Senda, T., Yuan, J., Cheng, Y.L., Bush, E.C., Dogra, P., Thapa, P., et al. (2019). Single-cell transcriptomics of human T cells reveals tissue and activation signatures in health and disease. Nat. Commun. *10*, 4706.

Tan, G., and Lenhard, B. (2016). TFBSTools: an R/bioconductor package for transcription factor binding site analysis. Bioinformatics *32*, 1555–1556.

Tirosh, I., Izar, B., Prakadan, S.M., Wadsworth, M.H., 2nd, Treacy, D., Trombetta, J.J., Rotem, A., Rodman, C., Lian, C., Murphy, G., et al. (2016). Dissecting the multicellular ecosystem of metastatic melanoma by single-cell RNA-seq. Science *352*, 189–196.

Traag, V.A., Waltman, L., and van Eck, N.J. (2019). From Louvain to Leiden: guaranteeing well-connected communities. Sci. Rep. *9*, 5233.

Vavrek, M. (2011). Fossil: palaeoecological and palaeogeographical analysis tools. Palaeontol. Electron. *14*, 16.

Virtanen, P., Gommers, R., Oliphant, T.E., Haberland, M., Reddy, T., Cournapeau, D., Burovski, E., Peterson, P., Weckesser, W., Bright, J., et al. (2020). SciPy 1.0: fundamental algorithms for scientific computing in Python. Nat. Methods *17*, 261–272.

Wakim, L.M., Woodward-Davis, A., Liu, R., Hu, Y., Villadangos, J., Smyth, G., and Bevan, M.J. (2012). The molecular signature of tissue resident memory CD8 T cells isolated from the brain. J. Immunol. *189*, 3462–3471.

Waskom, M., Botvinnik, O., O'Kane, D., Hobson, P., Lukauskas, S., Gemperline, D.C., Augspurger, T., Halchenko, Y., Cole, J.B., and Warmenhoven, J. (2017). Mwaskom/Seaborn: V0. 8.1 (September 2017). Zenodo.

Webb, J.R., Milne, K., Watson, P., Deleeuw, R.J., and Nelson, B.H. (2014). Tumor-infiltrating lymphocytes expressing the tissue resident memory marker CD103 are associated with increased survival in high-grade serous ovarian cancer. Clin. Cancer Res. *20*, 434–444.

Wolf, F.A., Angerer, P., and Theis, F.J. (2018). SCANPY: large-scale single-cell gene expression data analysis. Genome Biol. *19*, 15.

Wolf, F.A., Hamey, F.K., Plass, M., Solana, J., Dahlin, J.S., Göttgens, B., Rajewsky, N., Simon, L., and Theis, F.J. (2019). PAGA: graph abstraction reconciles clustering with trajectory inference through a topology preserving map of single cells. Genome Biol. *20*, 59.

Workel, H.H., Lubbers, J.M., Arnold, R., Prins, T.M., van der Vlies, P., de Lange, K., Bosse, T., van Gool, I.C., Eggink, F.A., Wouters, M.C.A., et al. (2019). A transcriptionally distinct CXCL13(+)CD103(+)CD8(+) T-cell population is associated with B-cell recruitment and neoantigen load in human cancer. Cancer Immunol. Res. *7*, 784–796.

Wu, J., Madi, A., Mieg, A., Hotz-Wagenblatt, A., Weisshaar, N., Ma, S., Mohr, K., Schlimbach, T., Hering, M., Borgers, H., and Cui, G. (2020). T cell factor 1 suppresses CD103+ lung tissue-resident memory T cell development. Cell Rep. *31*, 107484.

Xia, H., Wang, W., Crespo, J., Kryczek, I., Li, W., Wei, S., Bian, Z., Maj, T., He, M., Liu, R.J., et al. (2017). Suppression of FIP200 and autophagy by tumor-derived lactate promotes naive T cell apoptosis and affects tumor immunity. Sci. Immunol. *2*, eaan4631.

Zhu, H., Bengsch, F., Svoronos, N., Rutkowski, M.R., Bitler, B.G., Allegrezza, M.J., Yokoyama, Y., Kossenkov, A.V., Bradner, J.E., Conejo-Garcia, J.R., and Zhang, R. (2016). BET bromodomain inhibition promotes anti-tumor immunity by suppressing PD-L1 expression. Cell Rep. *16*, 2829–2837.

Zsiros, E., Duttagupta, P., Dangaj, D., Li, H., Frank, R., Garrabrant, T., Hagemann, I.S., Levine, B.L., June, C.H., Zhang, L., et al. (2015). The ovarian cancer chemokine landscape is conducive to homing of vaccine-primed and CD3/CD28-costimulated T cells prepared for adoptive therapy. Clin. Cancer Res. *21*, 2840–2850.

STAR★METHODS

KEY RESOURCES TABLE

REAGENT or RESOURCE	SOURCE	IDENTIFIER
Antibodies		
Mouse anti-human CD3	ThemoFisher Scientific	Thermo Fisher Scientific Cat# MA5-14524, Clone SP7; RRID: AB_10982026
Mouse anti-human CD8	DAKO	Agilent Cat# M7103, Clone C8/144B; RRID: AB_2075537
Rabbit monoclonal anti-human CD69	ABCAM	Clone EPR21814, Cat# ab233396
Rabbit monoclonal anti-human CD103	ABCAM	Clone SP301, Cat# ab227697
Rabbit monoclonal anti-human TCF1/7	CST	Cell Signaling Technology Cat# 2203, Clone C63D9; RRID: AB_2199302
Mouse anti-human PCK	DAKO	Agilent Cat# M3515, Clone AE1/AE3; RRID: AB_2132885
Rabbit anti-human CLEC9A	Abcam	Abcam Cat# ab223188, Clone EPR22324; RRID: AB_2884022
anti-mouse CD45.1	BioLegend	BioLegend Cat# 110736, Clone A20; RRID: AB_2562564
anti-mouse CD45.2	Tonbo Biosciences	Tonbo Biosciences Cat# 65-0454, Clone 104; RRID: AB_2621894
Hamster anti-mouse CD3e	BD Biosciences	BD Biosciences Cat# 563565, Clone 145-2C11; RRID: AB_2738278
Rat anti-mouse CD8a	BD Biosciences	BD Biosciences Cat# 551516, Clone 53-6.7; RRID: AB_398512
Anti-mouse CD69	Tonbo Biosciences	Tonbo Biosciences Cat# 60-0691, Clone H1.2F3; RRID: AB_2621856
Rat anti-mouse CD103	BD Biosciences	BD Biosciences Cat# 557495, Clone M290; RRID: AB_396732
Rat anti-mouse CD127	BD Biosciences	BD Biosciences Cat# 612841, Clone SB/199; RRID: AB_2870163
Rat anti-mouse CD186 (CXCR6)	BioLegend	BioLegend Cat# 151117, Clone SA051D1; RRID: AB_2721700
Mouse anti-human CD45	BD Biosciences	BD Biosciences Cat# 563716, Clone H130; RRID: AB_2716864
Mouse anti-human CD3	Tonbo Biosciences	Tonbo Biosciences Cat# 65-0037, Clone OKT3; RRID: AB_2621873
Mouse anti-human CD8	BD Biosciences	BD Biosciences Cat# 564628, Clone SK1; RRID: AB_2744464
Mouse anti-human CD69	BioLegend	BioLegend Cat# 310942, Clone FN50; RRID: AB_2564277
Mouse anti-human CD103 (Integrin alpha E)	BioLegend	BioLegend Cat# 350205, Clone Ber-ACT8; RRID: AB_10642026
Mouse anti-human CD49a (Integrin a1 chain)	BD Bioscience	BD Biosciences Cat# 742360, Clone SR84; RRID: AB_2740718
Mouse anti-human CD326 (Ep-CAM)	BioLegend	BioLegend Cat# 324244, Clone 9C4; RRID: AB_2750489
Mouse anti-human CD326 (Ep-CAM)	BioLegend	BioLegend Cat# 324205, Clone 9C4; RRID: AB_756079
Mouse anti-human CD27	BD Biosciences	BD Biosciences Cat# 560612, Clone M-T271; RRID: AB_1727457
Mouse anti-human CD279 (PD-1)	BioLegend	BioLegend Cat# 367422, Clone NAT105; RRID: AB_2721517

(*Continued on next page*)

Continued

REAGENT or RESOURCE	SOURCE	IDENTIFIER
Mouse anti-human CD279 (PD-1)	BioLegend	BioLegend Cat# 329951, Clone EH12.2H7; RRID: AB_2566363
Mouse anti-human CD127 (IL-7Ralpha)	BioLegend	BioLegend Cat# 351310, Clone A019D5; RRID: AB_10960140
Mouse anti-human CD38	BD Biosciences	BD Biosciences Cat# 560677, Clone HIT2; RRID: AB_1727473
Mouse anti-human CD366 (Tim-3)	BioLegend	BioLegend Cat# 345028, Clone F38-2E2; RRID: AB_2565829
Mouse anti-human CD39	BD Biosciences	BD Biosciences Cat# 563681, Clone TU66; RRID: AB_2738370
Rat anti-human CD197 (CCR7)	BD Biosciences	BD Biosciences Cat# 740267, Clone 3D12; RRID: AB_2740009
Rat anti-human TOX	Thermo Fisher Scientific	Thermo Fisher Scientific Cat# 50-6502-82, Clone TXRX10; RRID: AB_2574265
Rabbit anti-humna TCF1/TCF7	CST	Cell Signaling Technology Cat# 6709, Clone C63D9; RRID: AB_2797631
Mouse anti-human TCRalpha/beta	BioLegend	BioLegend Cat# 306718, Clone IP26; RRID: AB_10612569
Mouse anti-human HLA-A2	BioLegend	BioLegend Cat# 343320, Clone BB7.2; RRID: AB_2566767
Mouse anti-human CD8	BioLegend	BioLegend Cat# 344704, Clone SK1; RRID: AB_1877178
Anti-mouse H-2kb bound to SIINFEKL antibody	BioLegend	BioLegend Cat# 141603, Clone 25-D1.16; RRID: AB_10897938
Rat anti-mouse I-A/I-E	BD Biosciences	BD Biosciences Cat# 742894, Clone M5/114.15.2; RRID: AB_2734759
Rat IgG2a kappa Isotype Control	Thermo Fisher Scientific	Thermo Fisher Scientific Cat# 50-4321-82, Clone eBR2a; RRID: AB_10598503
Rabbit IgG Isotype Control	CST	Cell Signaling Technology Cat# 3452; RRID: AB_10695811
Bacterial and virus strains		
One Shot™ TOP10 Chemically Competent E.coli	ThermoFisher Scientific	Cat# C404010
Biological samples		
Human ovarian carcinoma tissues	H. Lee Moffitt Cancer Center	N/A
Human ovarian carcinoma tissues	Darmouth-Hitchcock Medical Center	N/A
Ovarian tumor tissue microarrays (TMAs)	Tissue Core at Moffitt Cancer Center	N/A
Ovarian tumor tissue microarrays (TMAs)	TriStar Technology Group, LLC	TA-1966
Ovarian tumor tissue microarrays (TMAs)	US BioMax, Inc.	Ov401sur
Chemicals, peptides, and recombinant proteins		
DMEM Medium	ThermoFisher Scientific	Cat# 11965092
Blasticidin S HCl, powder	ThermoFisher Scientific	R21001
RPMI 1640 Medium	Gibco™	Cat# 11875093
Penicillin/Streptomycin	Lonza	Cat# 17602E
L-glutamine	Genesee Scientific	Cat# 25509
Sodium pyruvate	ThermoFisher Scientific	Cat# 11360070
0.25% Trypsin-EDTA	Gibco™	Cat# 25200056
Dulbecco's Phosphate Buffered Saline 1X	VWR Life Science	Cat# 0201190500
jetPRIME Transfection reagent	Polyplus	Cat# 101000015
OVA-Q4H7 Peptide, pQ4H7, SIIQFEHL	AnaSpec	Cat# AS-64405
OVA-G4 Peptide, SIIGFEKL	AnaSpec	Cat# AS-64384
OVA Peptide (257-264), SIINFEKL	AnaSpec	Cat# AS-601931

(*Continued on next page*)

Continued

REAGENT or RESOURCE	SOURCE	IDENTIFIER
hgp100(25-33)	GenScript	Cat# RP20344
Recombinant Human IL-2	PeproTech	Cat# 200-02-50
Gamma-Globulins from Human Blood	Sigma	Cat# G4386
DAPI	Sigma	Cat# 8417
eBioscience™ Foxp3 / Transcription Factor Staining Buffer Set	Invitrogen	Cat# 00552300
SuperScript™ IV Reverse Transcriptase	Invitrogen	Cat# 18090010
PlatinumII *Taq* Hot-Start DNA Polymerase	Invitrogen	Cat# 14966001
POLYBRENE, 10MG/ML AQUEOUS SOLUTION	ThermoFisher Scientific	Cat# AB01643-00001
Lipofectamine™ 3000 Transfection reagent	Invitrogen	Cat# L3000015
RetroNectin reagent	Takara Bio	Cat# T100B
PMA	Invivogen	Cat# tlrl-pma
SYBR™ Select Master Mix	Applied Biosystems	Cat# 4472897
Zombie Yellow Fixable Viability Kit	BioLegend	Cat# 423104
TruStain FcX™ (anti-mouse CD16/CD32)	BioLegend	BioLegend Cat# 101320, Clone 93; RRID: AB_1574975
DRAQ5	BioLegend	Cat# 424101
Critical commercial assays		
Human IL-2 ELISA MAX Deluxe	BioLegend	Cat# 431804
EasySep™ Mouse CD8$^+$ T Cell Isolation Kit	STEMCELL	Cat# 19853
Tumor Dissociation Kit, mouse	Miltenyi	Cat# 130096730; Miltenyi Mouse Tumor Dissociation Kit, RRID: SCR_020285
RNeasy Mini kit	Qiagen	Cat# 74106
DNeasy Blood & Tissue Kit	Qiagen	Cat# 69504
ImmunoSEQ humanTCRB kit	Adaptive Biotech	N/A
KAPA Library Quantification Kits	Roche	N/A
NuGEN Ovation SoLo RNA-Seq library preparation kit	Tecan	N/A
Chromium™ Next GEM Single Cell 5' Library and Gel Bead Kit v1.1	10x Genomics	Cat#1000165
Chromium™ Single Cell V(D)J Enrichment Kit, Human T Cell	10x Genomics	Cat#1000005
Chromium™ Single Cell 5' Library Construction Kit	10x Genomics	Cat# 1000020
Chromium™ Next GEM Chip G Single Cell Kit	10x Genomics	Cat# 1000127
Chromium Next GEM Single Cell Multiome ATAC + Gene Expression Reagent Bundle	10x Genomics	Cat# 1000285
Chromium Next GEM Chip J Single Cell Kit	10x Genomics	Cat# 1000230
Automated OPAL 7-Color IHC kit	Akoya Biosciences	Cat# NEL821001KT
Deposited data		
Raw and processed bulk-RNAseq data in TRM vs. re-circulating CD8$^+$ TILs sorted from 7 HGSOC patients	This paper	GEO: GSE194383
Raw and processed single cell RNA-seq and VDJ data in TRM vs. re-circulating CD8$^+$ TILs sorted from 4 HGSOC patients	This paper	GEO: GSE193371
Raw and processed single cell multiome ATAC+GEX data in TRM vs. re-circulating CD8$^+$ TILs sorted from 4 HGSOC patients	This paper	GEO: GSE192780
Raw and processed single cell RNA-seq and VDJ data in TRM CD8$^+$ TILs sorted from 8 HGSOC patients	This paper	GEO: GSE194105

(*Continued on next page*)

Continued

REAGENT or RESOURCE	SOURCE	IDENTIFIER
Experimental models: Cell lines		
K-562	ATCC	ATCC Cat# CCL-243; RRID: CVCL_0004
HEK293T	ATCC	ATCC Cat# CRL-3216; RRID: CVCL_0063
Phoenix-AMPHO	ATCC	ATCC Cat# SD-3443; RRID: CVCL_H716
Jurkat76	Dr. Mirjam H. Heemskerk (University of Leiden)	N/A
UPK10	PMID: 22351930	N/A
Tumor1-sorted $CD45^{-}EpCAM^{+}$ primary HGSOC cells	This manuscript	N/A
Tumor2-sorted $CD45^{-}EpCAM^{+}$ primary HGSOC cells	This manuscript	N/A
293GP	N/A	RRID: CVCL_E072
Experimental models: Organisms/strains		
Mouse: B6.SJL-*Ptprc*^{a}*Pepc*^{b}/BoyCrCrl	Charles River Laboratory	RRID: IMSR_CRL:564
Mouse: C57BL/6-Tg(TcraTcrb)1100Mjb/J	The Jackson Laboratory	Cat# JAX:003831; RRID: IMSR_JAX:003831
Mouse: B6.Cg-*Thy1*^{a}/Cy Tg(TcraTcrb) 8Rest/J	The Jackson Laboratory	Cat# JAX:005023; RRID: IMSR_JAX:005023
Oligonucleotides		
Forward Cloning GP100: 5′- AAAAAAA AGAATTCGCCGCCACCATGGGTGTCC AGAGAAGGAGC-3′	Integrated DNA Technologies IDT	N/A
Reverse Cloning GP100: 5′-AAAAAAA AGTTAACTCAGACCTGCTGTCC -3′	Integrated DNA Technologies IDT	N/A
Forward Cloning Ova: 5′- AAAAAA AAGAATTCGCCGCCACCATGG GCTCCATCGG-3′	Integrated DNA Technologies IDT	N/A
Reverse Cloning Ova: 5′- AAAAAAAA GTTAACTTAAGGGGAAACACATC-3′	Integrated DNA Technologies IDT	N/A
PCR-Forward for *GAPDH*: 5′-GAAGG TGAAGGTCGGAGTC-3′	Integrated DNA Technologies IDT	N/A
PCR-Reverse for *GAPDH*: 5′- GAA GATGGTGATGGGATTTC-3′	Integrated DNA Technologies IDT	N/A
PCR Forward for *EPCAM*: 5′-TGCAG GGTCTAAAAGCTGGT-3′	Integrated DNA Technologies IDT	N/A
PCR Reverse for *EPCAM*: 5′- CCC TATGCATCTCACCCATC-3′	Integrated DNA Technologies IDT	N/A
Recombinant DNA		
pLV-EF1a-IRES-Blast	Addgene	Cat# 85133; RRID: Addgene_85133
pcDNA3-deltaOVA	Addgene	Cat# 64595; RRID: Addgene_64595
pLVX-IRES-mCherry	Takara Bio	Cat# 631237
pLVX-IRES-ZsGreen	Takara Bio	Cat# 632187
pBMN-I-GFP	Addgene	Cat# 1736; RRID: Addgene_1736
pBMN-V19J20-I-GFP	GenScript	N/A
pBMN-V21J21-I-GFP	GenScript	N/A
pBMN-V26J26-I-GFP	GenScript	N/A
pBMN-V54J17-I-GFP	GenScript	N/A
pBMN-V45J40-I-GFP	GenScript	N/A
ORF of CD3 Complex: CD3D-T2A-CD3E-P2A-CD3G-E2A-CD3Z	Integrated DNA Technologies IDT	N/A
ORF of HLA-A2-restricted TCR for NY-ESO	Integrated DNA Technologies IDT	N/A
ORF of HLA-A2	Integrated DNA Technologies IDT	N/A

(*Continued on next page*)

Continued

REAGENT or RESOURCE	SOURCE	IDENTIFIER
pVLX-CD3Comple-IRES-mCherry	This manuscript	N/A
pLVX-HLAA2-IRES-ZsGreen	This manuscript	N/A
pBMN-NY-ESO-I-GFP	This manuscript	N/A
pMD2.G	Addgene	Cat# 12259; RRID: Addgene_12259
psPAX2	Addgene	Cat# 12260; RRID: Addgene_12260
RD114	Addgene	Cat# 17576; RRID: Addgene_17576
Software and algorithms		
FlowJo v10.7.2	FlowJo LLC	N/A
GraphPad Prism v9	GraphPad Software Inc.	N/A
Adobe Photoshop 2022	Adobe	N/A
Adobe Illustrator 2022	Adobe	N/A
ImmunoSEQ Analyzer software	Adaptive Biotechnologies	https://www.immunoseq.com/analyzer/
STAR v2.5.3a	Dobin et al., 2013	http://code.google.com/p/rna-star/
cutadapt v1.8.1	Martin, 2011	https://cutadapt.readthedocs.io/en/v1.8.1/
featureCounts v1.5.3	Liao et al., 2013	http://subread.sourceforge.net/
R 4.0.2	R Core Team, 2019	https://www.r-project.org/
ComplexHeatmap v2.7.8 (R package)	Gu et al., 2016	https://www.bioconductor.org/packages/release/bioc/html/ComplexHeatmap.html
EnhancedVolcano v1.9.13 (R package)	Bioconductor	https://github.com/kevinblighe/EnhancedVolcano
CellRanger v5.0	10x Genomics	http://10xgenomics.com/
Seurat v4.0 (R package)	Stuart et al., 2019	https://satijalab.org/seurat/
AUCell (R package)	Aibar et al., 2017	https://github.com/aertslab/AUCell
Scanpy 1.8.2	Wolf et al., 2018	https://github.com/theislab/Scanpy
Cell Ranger VDJ v3.0	10x Genomics	http://10xgenomics.com/
UpsetR (R package)	Conway et al., 2017	https://github.com/hms-dbmi/UpSetR
fossil (R package)	Vavrek, 2011	https://cran.r-project.org/web/packages/fossil/index.html
Signac v1.3.0 (R package)	Stuart et al., 2020	https://docs.signac.io/projects/core/en/v1.3.0/
harmony (R package)	Korsunsky et al., 2019	https://github.com/immunogenomics/harmony
JASPAR2020 v0.99 (R package)	JASPAR	http://bioconductor.org/packages/release/data/annotation/html/JASPAR2020.html
TFBStools v1.31.2 (R package)	Tan and Lenhard, 2016	https://github.com/ge11232002/TFBSTools
fgsea (R package)	Korotkevich et al., 2021	https://github.com/ctlab/fgsea
GSEA 4.0.2	Subramanian et al., 2005	https://www.gsea-msigdb.org/gsea/index.jsp
spatstat (R package)	Baddeley and Turner, 2006	https://spatstat.org/
Python	Python 3.7	https://www.python.org/downloads/
leidenalg (Python package)	Traag et al., 2019	https://github.com/vtraag/leidenalg
Scipy (Python package)	Virtanen et al., 2020	https://docs.scipy.org/doc/
scikit-learn (Python package)	Pedregosa et al., 2011	https://scikit-learn.org/stable/
matplotlib (Python package)	Hunter, 2007	https://matplotlib.org/
seaborn (Pythonpackage)	Waskom et al., 2017	https://seaborn.pydata.org/
tifffile (Python package)	https://pypi.org/project/tifffile/	https://github.com/cgohlke/tifffile/

RESOURCE AVAILABILITY

Lead contact

Further information and requests for resources and reagents should be directed to and will be fulfilled by the lead contact, Jose R. Conejo-Garcia (jose.conejo-garcia@moffitt.org).

Materials availability

This study did not generate new unique reagents.

Data and code availability

Raw and processed bulk-RNAseq data of this study can be obtained from Gene Expression Omnibus (GEO) with an accession number of GEO: GSE194383. Raw and processed single cell RNA-seq and VDJ data (from both analysis, 4 HGSOC and 8 HGSOC) can be obtained from GEO with an accession numbers of GEO: GSE193371 and GSE194105. Raw and processed single cell multiome ATAC+GEX data of this study can be obtained from GEO with an accession number of GEO: GSE192780. The 4 datasets can be found with the accession number of SuperSeries GEO: GSE195486. Microscopy data reported in this paper will be shared by the lead contact upon request. This paper does not report original code; the modified scripts used for the spatial analysis are available upon request. Any additional information required to reanalyze the data reported in this paper is available from the lead contact upon request.

EXPERIMENTAL MODEL AND SUBJECT DETAILS

Human samples

Human high grade serous ovarian carcinoma (HGSOC) tissues were procured under protocols approved by the Committee for the Protection of Human Subjects at Dartmouth–Hitchcock Medical Center (no. 17702); under a protocol approved by the H. Lee Moffitt Cancer Center (MCC no. 18974). Patients were female in gender and their ages ranged from 23-85 with a median value of 57. Informed consent was obtained from all them. Tumor chunks were either freshly dissociated and cryopreserved; or freshly dissociated, sorted ($CD45^{-}EpCAM^{+}$ primary HGSOC cells) and cultured continuously in R10 medium (RPMI-1640, 10% FBS, penicillin/Streptomycin (100 μg/mL Lonza), l-glutamine (2 mM, Genesee Scientific), sodium pyruvate (0.5 mM) (ThermoScientific)) until they adhered to establish primary HGSOC cell lines. Established cell lines were used for subsequent experiments.

Ovarian tumor tissue microarrays (TMAs) were obtained from 3 different resources: the Tissue Core at Moffitt Cancer Center (MCC cohort; approval MCC no. 50264) which include 93 HGSOC and some control tissues; TriStar Technology Group, LLC (TA-1966, Rockville, MD), which include 51 HGSOC; and US BioMax, Inc. (Ov401sur; Derwood, MD) with 8 HGSOC.

Cell lines

K562 cells (ATCC Cat# CCL-243, RRID:CVCL_0004), HEK293T cells (ATCC Cat# CRL-3216, RRID:CVCL_0063) and Phoenix-AMPHO cells (ATCC Cat# SD-3443, RRID:CVCL_H716) were purchased from ATCC (Manassas, VA). Jurkat76 cells were provided by Mirjam H. Heemskerk (Department of Hematology, University of Leiden, Leiden, Netherlans). UPK10 cells are a p53/Kras-driven ovarian carcinosarcoma cell line (Rutkowski et al., 2015; Scarlett et al., 2012; Zhu et al., 2016).

K562, UPK10, Jurkat76 and established tumors were routinely cultured in R10 medium. For transduced UPK10, Blasticidine (ThermoFisher, R21001) was added to the medium (6ug/mL). HEK293T cells and Phoenix-AMPHO were cultured in D10 medium (DMEM, 10% FBS, penicillin/Streptomycin (100 μg/mL Lonza), l-glutamine (2 mM, Gen Clone), sodium pyruvate (0.5 mM)).

Animal models

For mouse models, three different strains were used. B6.Cg-Thy1a/Cy Tg(TcraTcrb)8Rest/J (Pmel) mice (RRID:IMSR_JAX:005023), 8-12 weeks old females, purchased from the Jackson Laboratory; C57BL/6-Tg(TcraTcrb)1100Mjb/J (OT-I) mice (RRID:IMSR_JAX:003831), 8-12 weeks old females, also purchased from Jackson Laboratory; and C57BL/6-Ly5.1/Cr mice (RRID:IMSR_CRL:564), 6-8 weeks old female, purchased from Charles River Laboratory. All animals were maintained by the animal facility of the Moffitt Cancer Center, housed in cages of up to 5 mice per cage, in a temperature controlled (18-23°C), 40-60% humidity, 12 h light/dark cycle facility. Animal studies were performed in accordance with Institutional Animal Care and Use Committee at the University of South Florida Research Integrity and Compliance department (IACUC protocols#IS00006655 and #IS00009457).

METHOD DETAILS

Constructs

The sequence of GP100 was obtained by PCR amplification from cDNA of B16 melanoma cell line using primers flanked by 5′EcoRI (5′- AAAAAAAAGAATTCGCCGCCACCATGGGTGTCCAGAGAAGGAGC-3′) and 3′HpaI (5′-AAAAAAAAGTTAACTCAGACCTGCT GTCC -3′) restrictions sites to clone it into pLV-EF1a-IRES-Blast backbone (Addgene #85133; RRID: Addgene 85133). The OVA-deltaN lacking the first 49 amino acids was cloned from pcDNA3-deltaOVA (Addgene 64595; RRID:Addgene_64595) into pLV-EF1a-IRES-Blast backbone by PCR amplification and using 5′EcoRI (5′- AAAAAAAAGAATTCGCCGCCACCATGGGCTC

CATCGG-3′) and 3′HpaI (5′- AAAAAAAAGTTAACTTAAGGGGAAACACATC-3′) restrictions sites.

The ORF of CD3 complex was purchased from IDT (Coralville, IA) as a sequence of CD3D-T2A-CD3E-P2A-CD3G-E2A-CD3Z flanked by 5′ EcoRI and 3′ Not-I restrictions sites. They sequence was then ligated into pLVX-IRES-mCherry (Takara Bio USA) by standard cloning techniques. The sequence corresponding to an HLA-A2-restricted TCR that recognizes SLLMWITQC, corresponding to residues 157 to 165 of NY-ESO-1 (publicly available http://www.google.com/patents/US8143376) was purchased from IDT and ligated into pBMN-I-GFP (Addgene # 1736; RRID: Addgene 1736). The retroviral vectors for expressing the αβ-TCRs obtained from the VDJprofile analysis from 2 different HGSOCs *(TRAV26-2/TRAJ26/TRAC*, *TRBV2/TRBD2/TRBJ2-3/TRBC2*; *TRAV17/TRAJ54/TRAC*, *TRBV4-1/TRBD1/TRBJ2-3/TRBC2*; *TRAV40/TRAJ45/TRAC*,*TRBV4-1/TRBD1/TRBJ2-3/TRBC2*; *TRAV19/TRAJ20/TRAC*, *TRBV2/TRBD2/TRBJ2-3/TRBC2*; *and TRAV21/TRAJ11/TRAC*,*TRBV28/TRBD2/TRBJ2-7/TRBC2)*, were purchased from Genscript (Piscataway, NJ) using pBMN-I-GFP as a backbone. Sequences corresponding to the ORF of HLA-A2 were purchased from IDT and ligated into pLVX-IRES-ZsGreen (Takara Bio USA). The sequence integrity and accuracy of all constructs was assessed and confirmed by sequencing services from GeneWiz.

The corresponding empty vectors (Mock) were used as a control in the different experiments.

Tumor models

UPK10 cells were lentivirally transduced to express Ovalbumin (OVA; OVAlow-UPK10), GP100 protein (GP100-UPK10), or the control vector (Mock, empty vector) and were used to establish subcutaneous flank tumors in C57BL/6-Ly5.1/Cr mice (B6.SJL-Ptprca-Pepcb/BoyCrCrl) by injecting 12×10^6 cells in 200ul PBS. Tumors establishment was allowed for 9 days. This was followed by intratumoral infusion of 2.5 $x10^6$ purified Pmel-$CD8^+$ or OT-I $CD8^+$ T cells that were activated 2 days prior with different peptides (gp100 (25-33) peptide, SIINFEKL, SIIQFEHL or SIIGFEKL), with SIINFEKL at different doses (0.5, 1 or 2μg/mL) or maintained with IL-2 (50U/mL) as a control. These tumors were allowed to grow for an additional 7 days before dissociation into a homogeneous single cell suspension using a Tumor Dissociation Kit from Miltenyi Biotech (CAT#130-096-730; RRID:SCR_020285). For analysis of TRM-like and re-circulating populations in peripheral blood, 400uL of blood was extracted by cardiac puncture in anesthetized mice prior to sacrifice. For analysis of draining lymph nodes, the lymph node closest to the tumor was taken. Blood and lymph nodes were processed into a single cell suspension and analyzed by FACS. Dissociated tumors were analyzed by FACS, sorted or frozen. TRM-like or re-circulating Pmel TILs or OT-I TILs were sorted and $2.5\text{-}3.0\times10^4$ cells were intratumorally injected in similar tumors to study tumor growth. The number of injected animals per experiment depended on the number of sorted cells, to inject comparable number of cells per tumor. Animals bearing subcutaneous tumors were randomized to ensure a similar size variability per group before injection of TRM-like or re-circulating TILs. To remove bias, a blind tumor measurement was done. Length, width, and height of tumors were measured (L,W, H) and volumes were calculated according to the ellipsoid volume formula ($V= 4/3\times\pi\times (L/2)\times(W/2)\times(H/2)$.

C57BL/6-Tg(TcraTcrb)1100Mjb/J (OT-I) mice were used to isolate splenocytes. The splenocytes were maintained in R10 medium and supplemented with IL-2 (control) 50 U/mL (PeproTech), or activated with 1 μg/mL SIINFEKEL, Q4H7 (SIIQFEHL) or G4 (SIIGFEKL) for 2 days for studies to compare activation by the different peptides, or with 0.5, 1 or 2μg/mL of SIINFEKL to study the differences between peptide concentrations. Then, the cultured $CD8^+$ OT-I cells were purified using EasySep™ Mouse $CD8^+$ T Cell Isolation Kit (Catalog # 19853) and intratumorally injected. The number of tumors injected depended on the number of isolated $CD8^+$ T cells to inject 2.5×10^6 purified $CD8^+$ OT-I cells/tumor.

B6.Cg-Thy1a/Cy Tg(TcraTcrb)8Rest/J (Pmel) mice were used to isolate splenocytes. The splenocytes were activated *in vitro* for 2 days using Gp100 (25-33) peptide and Pmel $CD8^+$ T cells were purified and intratumorally injected, 2.5 $x10^6$ cells/tumor.

Flow cytometry, sorting and ImageStream

Dissociated HGSOC were stained with DAPI, blocked with γ-globulin (Sigma, 4mg/mL in PBS) and stained for 60min at 4°C with the following antibodies: CD45 (BD Bioscience, HI30, 1:200, RRID:AB_2716864), CD3 (Tonbo, OKT3, 1:200, RRID:AB_2621873), CD8 (BD Bioscience, SK1, 1:200, RRID:AB_2744464), CD69 (Biolegend, FN50, 1:200, RRID:AB_2564277), CD103 (Biolegend, Ber-ACT8, 1:200, RRID:AB_10642026), CD49a (BD OptiBuild, SR84, 1:200, RRID:AB_2740718) and sorted on BD FACS ARIA. Cells were gated for TRM-like TILs ($CD45^+CD3^+CD8^+CD69^+CD103^+$) and for re-circulating TILs ($CD45^+CD3^+$ $CD8^+CD103^-$). The same antibodies that were used for sorting were used for FACS analysis. In addition, the following antibodies/reagents were used for flow cytometry analysis: Zombie Yellow (BioLegend) viability dye, EpCam (Biolegend, 9C4, 1:100, RRID:AB_2750489), CD27 (BD Bioscience, M-T271, 1:200, RRID:AB_1727457), CD39 (BD Biosciences, TU66, 1:200, RRID:AB_2738370), CD279 (PD-1, Biolegend, NAT105, 1:200, RRID:AB_2721517 and RRID:AB_2566363), CD127 (IL7Ra; Biolegend, A019D5, 1:200, RRID:AB_10960140), CD38 (BD Bioscience, HIT2, 1:200, RRID:AB_1727473), CD366 (TIM3; Biolegend, F38-2E2, RRID:AB_2565829), CD197 (CCR7; BD Bioscience, 3D12, 1:200, RRID:AB_2740009).

For intracellular staining we used eBioscience™ Foxp3 / Transcription Factor Staining Buffer Set (Invitrogen) and followed the instructions according to the manufacturer. The following antibodies were used: TOX (Invitrogen, TXTR10, 1:50, RRID:AB_2574265), and Rat IgG2a kappa Isotype (Invitrogen, eBR2a, 1:50, RRID:AB_10598503), TCF1/TCF7 (Cell signaling, C63D9, 1:50, RRID:AB_2797631) and Rabbit IgG Isotype Control (Cell signaling, 1:50, RRID:AB_10695811).

Ova^{low}-UPK10 tumors or GP100-UPK10 tumors were stained with Zombie Yellow (BioLegned) viability dye, blocking with anti-mouse CD16/32 (BioLegend, RRID:AB_1574975), and staining for 60 min at 4°C with the following anti-mouse antibodies: CD45.1 (Biolegend, A20, 1:200, RRID:AB_2562564), CD45.2 (Tonbo, 104, 1;200, RRID:AB_2621894), CD3 (BD Biosciences, 145-2C11, 1:200, RRID:AB_2738278), CD8 (BD Biosciences, 53-6.7, 1:200, RRID:AB_398512), CD69 (Tonbo, H1.2F3, 1:200,

RRID:AB_2621856), CD103 (BD Biosciences, M290, 1:200, RRID:AB_396732) for sorting. For analysis by flow cytometry we included CD127 (BD Biosciences, SB/199,1:200, RRID:AB_2870163), CXCR6 (BioLegend, SA051D1,1:200, RRID:AB_2721700), I-A/I-E (BD Biosciences, M5/114.15.2, 1:200, RRID:AB_2734759) and TCF1/TCF7 for intracellular staining.

For sorting OVA^{low} expression in UPK10 we used the antibody to detect SIINFEKL bound to H-2kb (Biolegend, 25-D1.16, 1:200, RRID:AB_10897938). The sorting of HLA:A2 aAPC was done using ZsGreen and with additional staining with antibody detecting HLA-A2 (Biolegend, BB7.2, 1:200, RRID:AB_2566767). For sorting of Jurkat76 expressing αβ-TCRs and CD3complex GFP was used and mCherry in addition to the antibody detecting αβ-TCR (Biolegend, IP26, 1;200, RRID:AB_10612569).

Anti-mouse and anti-human antibodies were directly fluorochrome-conjugated. Data was collected using BD FACS Diva v.8.0.1 and analyzed using FlowJo v.10.7.1. Gating strategies for mouse experiments were: TRM-like CD8$^+$ TILs (CD45.2$^+$CD3$^+$CD8$^+$CD69$^+$ CD103$^+$); re-circulaiting TILs (CD45.2$^+$CD3$^+$CD8$^+$CD103$^-$); TRMstem TILs (CD45.2$^+$CD3$^+$CD8$^+$CD69$^+$CD103$^+$IL7R$^+$TCF1$^+$); TRMeff TILs (CD45.2$^+$CD3$^+$CD8$^+$CD69$^+$CD103$^+$CXCR6$^+$MHCII$^+$).

For Trogocytosis analysis and imaging the Amnis Image Stream X MkII was used. Cells were stained with Dapi, CD45 (BD Bioscience, HI30, 1:200), CD3 (Tonbo, OKT3, 1:200), CD8(Biolegend, SK1, 1:200, RRID:AB_1877178), DRAQ5 (Biolegend, 1:1000), EpCam (Biolegend, 9C4, 1:100, RRID:AB_756079).

EPCAM expression analysis

Quantification of *EPCAM* expression was performed in sorted EpCAM$^+$CD3$^+$CD8$^+$ TILs and their corresponding tumors. The quantification was done by isolating total RNA using RNeasy Plus Micro Kit (Qiagen). RNA was reverse transcribed to cDNA using SuperScript-IV (Invitrogen) with random hexamers. Quantification of *EPCAM* and *GAPDH* mRNA levels was performed by PCR using PlatinumII *Taq* Hot-Start DNA Polymerase (Invitrogen) and the following primers: Forward *GAPDH*: 5′-GAAGGTGAAGGTCG GAGTC-3′; Reverse *GAPDH*: 5′- GAAGATGGTGATGGGATTTC-3′; Forward *EPCAM*: 5′-TGCAGGGTCTAAAAGCTGGT-3′; Reverse *EPCAM*: 5′- CCCTATGCATCTCACCCATC-3′. PCR products were run in an agarose gel. *GAPDH* mRNA was used as a house-keeping gene. *EPCAM* expression was also quantified by quantitative reverse-transcriptase real-time PCR in: 1) sorted CD3$^+$CD8$^+$ TILs and tumor cells from 3 independent tumors; 2) in sorted TRM-like CD8$^+$ TILs, re-circulating CD8$^+$ TILs and tumor cells from another 3 independent tumors. The reaction was performed using SYBR Green master mix reagent (Applied Biosystems) and the same primers and house-keeping gene, *GAPDH*.

T-cell receptor beta chain sequencing

TRM-like and re-circulating CD8$^+$ TILs were sorted form 12 different HGSOCs. Genomic DNA was isolated using DNeasy Blood & Tissue Kit (Qiagen) according to manufacturer recommendations. TCRβ sequencing was performed by the Moffitt Cancer Center Molecular Genomics facility. Survey level T-cell receptor repertoire analysis was carried out with the use of the Adaptive Biotechnologies immunoSEQ assay v3, which employs bias-controlled multiplex PCR amplification and high-throughput sequencing to target rearranged T-cell receptor genes. Briefly, the manufacturer's protocol was followed in order to utilize the immunoSEQ hsTCRB kit to amplify the CDR3 locus from genomic DNA extracted from TRM-like and re-circulating CD8$^+$ TILs sorted from 12 HGSOCs. Following the confirmation of amplification and a successful final library preparation, sequencing was performed on the Illumina NextSeq 500 to a targeted depth of 2 million sequencing reads per sample. The data were analyzed using the Adaptive Biotechnologies Immunoseq Analyzer software, which identifies the V, D, and J genes, filters non-productive sequences, and reports and tracks T cell clonality.

Productive clonality is derived from the standard Shannon Entropy. Specifically for Adaptive Biotechnologies ImmunoSEQ Analyzer software, Entropy as shown in the Analyzer = -1 * the sum over all unique productive (in-frame) sequences of [(sequence count/total productive count) * log2(sequence count/total productive count)] normalized entropy (not shown in the Analyzer) = entropy / log2(productive unique in-frame sequences). Clonality as shown in the Analyzer = 1 - normalized entropy.

Bulk RNA-seq library and sequencing

TRM-like and re-circulating CD8$^+$ TILs were sorted form 7 different HGSOCs. Total RNA was isolated from sorted cells using RNA isolation kit (Qiagen) and analyzed for RINe. Next gen RNA sequencing was performed by the Moffitt Cancer Center Molecular Genomics facility.

One nanogram of RNA was processed for RNA-seq using the NuGEN Ovation SoLo RNA-Seq system. This low-input kit generates strand-specific libraries rRNA depleted libraries using an inline probe-based depletion step referred to as AnyDeplete. The cDNA was generated and libraries were prepared according to the manufacturer's protocol, including the optional inline DNase digestion step. Final libraries were quantitated with the Kapa Library Quantification kit and were sequenced on the Illumina NextSeq 500 in order to generate 8-10 million pairs of 75-base paired-end reads per sample.

Bulk RNA-seq data processing, normalization, differential expression, and gene set enrichment analysis

Paired-end RNA-seq reads were aligned to the GRCh37 human reference genome using STAR v2.5.3a (Dobin et al., 2013) following adaptor trimming by cutadapt v1.8.1 (Martin, 2011). Uniquely mapped reads were counted by featureCounts v1.5.3 (Liao et al., 2013) using Gencode V30 transcript annotations for human. Differential expression analysis was performed to compare TRM-like (n=7) vs re-circulating (n=7) TILs using DESeq2 with library size taken into consideration. Heatmaps were generated with R package ComplexHeatmap v2.7.8 (Gu et al., 2016) using z-score transformed log 2 (1 + normalized count). Bar plots were generated to visualize expression of individual genes in Transcripts Per Million (TPM) values. Volcano plot was generated with R package

EnhancedVolcano v1.9.13 using log 2 (1 + normalized count). Genes were further ranked based on –log10(p-value)*(sign of log2(fold-change)). The ranked gene list was used to perform pre-ranked gene set enrichment analysis (GSEA v4.0.2 (Subramanian et al., 2005)) to assess the enrichment of hallmarks, curated gene sets, and gene ontology (Ashburner et al., 2000) terms in MSigDB. The resulting normalized enrichment score (NES) and FDR controlled p-values were used to assess the transcriptome differences between TRM-like and re-circulating $CD8^+$ cells.

Single cell RNA-seq and VDJ profiling library and sequencing

TRM-like and re-circulating $CD8^+$ TILs were sorted form 4 different HGSOCs for TRM+re-circ scRNA-seq analysis. TRM-like $CD8^+$ TILs were sorted from 8 HGSOCs for TRM scRNA-seq analysis. Single-cell RNA-sequencing as performed using the 10X Genomics Chromium by the Moffitt Cancer Center Molecular Genomics facility. A single-cell suspension derived from dissociated tissue was sorted for Tumor-infiltrating lymphocytes and analyzed for viability using the Nexcelom Cellometer Auto 2K. The cell suspension was loaded onto the 10X Genomics Chromium Single Cell Controller at a concentration of one thousand cells per microliter in order to encapsulate between 2400 and 12,500 cells per sample. Briefly, the single cells, reagents, and 10x Genomics gel beads were encapsulated into individual nanoliter-sized Gelbeads in Emulsion (GEMs) and then reverse transcription of poly-adenylated mRNA was performed inside each droplet. The cDNA and VDJ-enriched libraries were completed in a single bulk reaction using the 10X Genomics Chromium NextGEM Single Cell 5′ v 1.1 and V(D)J Reagent Kits. 50,000 or 5,000 sequencing reads per cell for scRNA-seq or VDJ libraries, respectively, were generated on the Illumina NextSeq 500 instrument. Demultiplexing, barcode processing, alignment, and gene counting were performed using the 10X Genomics CellRanger v5.0 software.

Single-cell RNA-seq data processing, filtering, batch effect correction, and clustering

Raw sequencing reads from scRNA-seq were processed using Cell Ranger (v5.0, 10X Genomics). Briefly, the base call (BCL) files generated by Illumina sequencers were demultiplexed into fastq files based on the sequences of the sample index, and aligned against GRCh38 human transcriptome using STAR (Dobin et al., 2013). Cell barcodes and UMIs associated with the aligned reads were subjected to correction and filtering. Filtered gene-barcodes matrices containing only barcodes with UMI counts passing threshold for cell detection were imported to Seurat v4.0 (Stuart et al., 2019) for downstream analysis. Barcodes with fewer than 200 genes expressed or more than 10% UMIs originated from mitochondrial genes were filtered out; genes expressed in fewer than 3 barcodes were also excluded. This process resulted in 43,368 cells for TRM+re-circ scRNA-seq from 4 tumors, and 60,010 cells for TRM scRNA-seq from 8 tumors. For each sample, standard library size and log-normalization was performed on raw UMI counts using NormalizeData(), and top 5000 most variable genes were identified by the "vst" method in FindVariableFeatures(). Variable T cell receptor and immunoglobulin genes were removed from the variable gene list to prevent clustering based on V(D)J transcripts. S and G2/M cell cycle phase scores were assigned to cells based on previously defined gene sets(Tirosh et al., 2016) using CellCycleScoring() function.

In each study, individual data were further integrated to remove batch effects using an anchor-based method (Stuart et al., 2019) implemented in Seurat v4.0 using FindIntegrationAnchors() and IntegrateData() functions in Seurat with 10,000 "anchors" and top 40 principal components. Briefly, dimension reduction was performed on each data using diagonalized canonical correlation analysis (CCA) and L2-normalization was applied to the canonical correlation vectors to project the datasets into a shared space. The algorithms then searched for mutual nearest neighbors (MNS) across cells from different datasets to serve as "anchors" which encoded the cellular relationship between datasets. Finally, correction vectors were calculated from "anchors" and used to integrating datasets.

From the integrated data, scaled z-scores for each gene were calculated using ScaleData() function in Seurat by regressing against the percentage of UMIs originated from mitochondrial genes, S and G2/M phases scores, and total reads count. A shared nearest neighbor (SNN) graph was constructed based on the first 40 principal components computed from the scaled integrated data. Louvain clustering (Blondel et al., 2008) was performed using the FindClusters() function at resolution 1.2 for TRM+re-circ scRNA-seq data (28 clusters) and resolution 1.0 for TRM scRNA-seq data (26 clusters). Uniform manifold approximation and projection (UMAP) was used to visualize single-cell gene expression profile and clustering, using RunUMAP() function in Seurat with default settings. TRM module scores for individual cells were calculated from TRM-like core genes (Amsen et al., 2018; Corgnac et al., 2018; Hombrink et al., 2017; Kumar et al., 2017; Mueller and Mackay, 2016; Parga-Vidal et al., 2021; Szabo et al., 2019) using AddModuleScore() function in Seurat. Core up-regulated gene-set used: *ITGAE*, *CD69*, *ITGA1*, *CXCR3*, *CXCR6*, *CCR5*, *CCR6*, *CTLA4*, *HAVCR2*, *LAG3*, *EGR1*, *NR4A2*, *BATF*, *NAB1*, *RUNX3*, *NOTCH1*, *ZNF683*, *PRDM1*, *IFNG*, *GZMA*, *GZMB*, *SEMA7A*, *KLRB1*, *CCL3*, *STAT1*, *RAB27A*, *IL21R*, *FKBP1A*, *PRF1*, *TNF*, *NFKB1*, *CD44*, *BHLHE40*, *RBPJ*, *AHR*, *FABP1*, *PDCD1*, *GADD45A*, *TIGIT*, *CXCL10*, *NR4A3*, *FASLG*, *NR4A1*, *NR4A2*. Core down-regulated gene-set used: *CX3CR1*, *CCR7*, *SELL*, *S1PR1*, *KLF2*, *EOMES*, *TCF7*, *TBX21*.

Differential gene expression analysis and cluster annotation

Differential expression analysis was performed using FindAllMarkers() function in Seurat with logfc.threshold=0.25, min.pct=0, and test.use="wilcox". Cells within each cluster were compared against all other cells. Genes with Bonferroni-corrected p-value <0.05 and an average log-fold change > 0.25 and were considered differentially expressed. Results from differential gene expression analysis were provided in Tables S2 and S4. Clusters were annotated by comparing differential genes with markers previously associated with T cell stemness/memory (*SELL*, *TCF7*, *IL7R*, *CD28*, *CCR7*, *CD27*, *CXCR5*), effector activity (*GZMB*, *GNLY*, *PRF1*, *IFNG*), proliferation (*STMN1*, *CDK1*, *DNMT1*), and exhaustion/dysfunction (*PDCD1*, *HAVCR2*, *TIGIT*, *CTLA4*). Enrichment scores of T cell exhaustion gene set (*TOX*, *LAG3*, *PDCD1*, *HAVCR2*, *ITGAE*, *TIGIT*, *CXCL13*) and T cell stemness gene set (*TCF7*, *CDCR5*, *CD28*,

GZMK, *CCR7*, *IL7R*, *BCL6*, *SELL*, *CD27*) were calculated using AUCell algorithm implemented in SCENIC(Aibar et al., 2017). Cell proliferation scores were assessed based on the percentage of UMIs originated from genes related to the G2/M cell cycle phase (Tirosh et al., 2016). Briefly, a density distribution was fitted for proliferation scores across all cells and a cut-off value that separated the two density peaks was identified. Then, the percentage of cells with proliferation scores > the cutoff was calculated and evaluated for each cluster to identify proliferative clusters. After annotation, clusters were further merged into major groups based on cluster annotations and cell types (TRM-like vs re-circulating cells) for further analysis (see Figure S2 for TRM+re-circ scRNA-seq data and Figure S6 for TRM scRNA-seq data).

Visualization of marker genes on singe cell RNA-seq clusters and groups

Marker genes were visualized on UMAP projections or violin plots using log-normalized counts. For bubble plot of marker genes, the average expression of each gene was calculated for each cluster/group and then normalized by mean and standard deviation (z-scores).

Trajectory analysis

A partition-based graph abstraction (PAGA) algorithm (Wolf et al., 2019) implemented in single cell RNA-seq analysis package Scanpy (Wolf et al., 2018) was used to assess the differentiation trajectory for $CD8^+$ TRM-like cells. UMAP dimensionality reduction was performed on batch effects corrected PCs extracted from Seurat and a kNN-like graph at the major group level was constructed using the default settings. High-connectivity edges with weights higher than 0.1 were drawn on the graph.

Gene set enrichment analysis of major groups

To systematically identify differences between major groups on the trajectory, we performed gene set enrichment analysis utilizing the differential expression results of each group. For each group, genes were ranked based on -log10(p-value)*(sign of log2(fold-change)), with most up-regulated genes at the top and most down-regulated genes at the bottom. Pre-ranked gene set enrichment analysis (GSEA) was performed on ranked genes using R package fgsea (Korotkevich et al., 2021) with 10,000 permutations. The Hallmarks, KEGG, BIOCARTA, REACTOME, PID, Gene Ontology, ImmuneSigDB databases from MsigDB (Godec et al., 2016; Liberzon et al., 2011, 2015; Subramanian et al., 2005) were used as gene sets.

Single cell TCR-seq clonotype analysis

TCR reads sequenced by V(D)J assay were aligned to GRCh38 reference transcriptome using Cell Ranger VDJ (v3.0, 10X Genomics). T cells were assigned with productive CDR3 regions for TCR alpha and TCR beta chains. Each clonotype was assigned with a unique identifier based on amino acid sequences of the CDR3 regions and V(D)J genes of the two chains, which were then used to match clonotypes across samples. Clonotypes overlapped between major groups were visualized using R package UpsetR (Conway et al., 2017). Trajectory of the top clonotypes was visualized on UMAP projection generated from the paired scRNA-seq data (Figures 4F and S3I).

Within-cluster, within-group, and within-sample clonalities were calculated from normalized Shannon index: Shannon Clonality = $1 - \frac{-\sum_{i=1}^{R} P_i log_2[P_i]}{log_2 R}$, where R= the total number of clonotypes; i= each clonotype; P_i = percentage of cells with clonotype i among all cells. The Shannon Clonality ranges from 0 – 1, and the higher the value the more oligoclonal the sample.

Between-cluster and between-group clonotype similarity was measured by Morisita-Horn similarity index (Rempala and Seweryn, 2013) using R package fossil (Vavrek, 2011). This index compares overlap between clonotypes of two samples and ranges from 0 (no overlap) and 1 (complete overlap).

Single cell multiome ATAC+GEX library and sequencing

TRM-like and re-circulating $CD8^+$ TILs were sorted from 4 different HGSOCs. Paired single-cell RNA-sequencing and ATAC-sequencing was performed using the 10X Genomics Chromium system by the Moffitt Cancer Center Molecular Genomics facility. Single-cell suspensions of TRM-like and re-circulating TILs were analyzed for viability using the Nexcelom Cellometer K2. Cells were lysed and nuclei were isolated and diluted in buffer according to the manufacturer's protocol. The nuclei were transposed in bulk and the nuclei suspension was loaded onto the 10X Genomics Chromium Single Cell Controller in order to encapsulate between 400 and 20,000 nuclei per sample. Briefly, the nuclei, reagents, and 10x Genomics gel beads were encapsulated into individual nano-liter-sized Gelbeads in Emulsion (GEMs) and then reverse transcription of poly-adenylated mRNA and 10X barcode attachment of transposed DNA were performed inside each droplet. Following pre-amplification, the cDNA and ATAC-seq libraries were completed in a single bulk reaction using the 10X Genomics Chromium NextGEM Single Cell Multiome ATAC + Gene Expression Reagent Kit. 50,000 or 25,000 sequencing reads per cell for scRNA-seq or ATAC-seq libraries, respectively, were generated on dedicated Illumina NextSeq 500 sequencing runs according to the vendor protocol. Demultiplexing, barcode processing, alignment, and gene counting were performed using the 10X Genomics CellRanger v6.0 software.

Single cell multiome ATAC + GEX data processing, filtering, batch effect correction and clustering analysis

Raw sequencing reads generated from 10X multimode assay were processed by cellranger-arc workflow with default settings to generate mapping and chromatin accessibility data for ATAC and filtered UMI count data for GEX. The UMI count data for gene

expression was imported to Seurat v4.0 (Stuart et al., 2019). Filtering, batch effect correction, normalization, clustering, and differential expression analysis were performed as described above (see STAR Methods for scRNA-seq analysis). A total of 25 clusters were identified from 20,866 TRM-like+re-circ cells from 4 tumors by FindClusters() function in Seurat with resolution = 1. These clusters were further matched to the major groups identified in TRM+re-circ scRNA-seq data based on their marker gene expression (see Figure S4).

The mapping and chromatin accessibility data generated from Multiome ATAC were imported to R package Signac v1.3.0 (Stuart et al., 2020) for downstream analysis. The low-quality cells with total number of fragments in peaks < 3000 or > 20,000, fraction of fragments in peaks < 15%, ratio of mononucleosomal to nucleosome-free fragments > 4, or transcriptional start site (TSS) enrichment score < 2 were filtered out. A latent semantic indexing (LSI) dimension reduction was performed on the filtered cells. Briefly, peaks data were normalized by the frequency-inverse document frequency (TF-IDF) method using RunTFIDF() function in Signac to correct for differences in sequencing depth across cells and across peaks. Only peaks presented in more than 20 cells were selected for dimension reduction. Then a singular value decomposition (SVD) dimension reduction was performed on the TF-IDF matrix using the selected peaks followed by Harmony batch correction using RunHarmony() function implemented in R package harmony (Korsunsky et al., 2019). Next, a UMAP projection was generated using the first 40 reduced dimensions as input. Cells were assigned into major groups based on their grouping information obtained from multiome GEX data (see above).

Gene activity scores

The concept of gene activity is based on the observation that gene expression level is often correlated with chromatin accessibility at the gene body, promoter, and distal regulatory elements (Granja et al., 2019; Pliner et al., 2018). A gene activity matrix was created by counting reads mapped to gene body and promoter regions (extended 2kb upstream from gene coordinates) using GeneActivity() function in Signac, and further log-normalized using NormalizeData() function in Seurat with default settings. Differential expression analysis was performed on the normalized gene activity scores for each group. Genes with Bonferroni-corrected p-value < 0.05 and an average log-fold change > 0.25 were considered differentially expressed (Table S3) and visualized by R package ComplexHeatmap v2.7.8 (Gu et al., 2016).

Identification of group-specific peaks and TF motifs

The differential accessible peaks between groups were identified by logistic regression with the total number of fragments as a latent variable to correct for differential sequencing depth. Region satisfying the following criteria were considered differentially accessible: 1) Bonferroni-corrected p-value < 0.05, 2) an average log-fold change > 0.25, 3) and at least 5% of the cells accessible at the region (Table S3). Differentially accessible regions were further annotated to their closet genes using ClosestFeature() function in Signac, and visualized by R package ComplexHeatmap v2.7.8 (Gu et al., 2016). To visualize individual accessible regions across different groups, pseudo-bulk accessibility tracks were generated by averaging signals from all cells within a group and plotted with CoveragePlot() function in Signac.

Transcription factor motif enrichment in differentially accessible regions between groups was performed in Signac. Frist, human motif position frequency matrices were retrieved from JASPAR database using R packages JASPAR2020 v0.99 and BSgenome.Hsapiens.UCSC.hg38 v1.4.3, and getMatrixSet() function in R package TFBStools v1.31.2 (Tan and Lenhard, 2016). Then a hypergeometric test was performed to test for motif enrichment by considering GC content in the accessible regions, and p-values were adjusted with Benjamini– Hochberg. The enrichment scores were calculated as $-log_{10}$ (adjusted p-value) and visualized by R package ComplexHeatmap v2.7.8.

Virus production and transduction

Lentiviral particles were generated by co-transfecting HEK 293T/17 (ATCC) with pLV-EF1a-IRES-Blast, pLVX-IRES-ZsGreen or pLVX-IRES-mCherry and packaging/envelope vector pMD2.G (RRID:Addgene_12259) and psPAX2 (RRID:Addgene_12260) using JetPrime reagents and the viral supernatant was harvested 48h after. $5x10^5$ UPK10, K562 or Jurkat76 cells were seeded in a 6-well plate with 3mL of the corresponding viral supernatant including 10 μg/mL polybrene (Millipore). The plates were spined for 90min at 32°C and 1200g. 12h after transduction the medium was changed to R10 and 48h later the expression of the target gene was verified by FACS analysis or immunoblotting.

Retrovirus was generated by co-transfecting 293GP (RRID:CVCL_E072) with pBMN-I-GFPvector and the RD114 (RRID:Addgene_17576) envelope vector using Lipofectamine 3000 (Invitrogen). We collected the supernatant containing the retroviral particles at 48h and 72h after transfection and used the supernatant for two repeated spin infections with Retronectin coated 6 well plates (Takara). $2x10^6$ Jurkat 76 were transduced per well and 12h after the transduction supernatant was removed and medium was changed to R10. Selection of Jurkat76 positive cells was performed by FACS sorting using GFP as a marker.

Co-culture of Jurkat76 and measurement of IL-2 production by ELISA

Jurkat76 cells were lentivirally transduced with CD3complex (pLVX-IRES-mCherry-CD3 complex) and retrovirally transduced with an αβTCR (pBMN-I-GFP-αβTCR). Then, they were co-cultured with the corresponding immortalized tumor cells (tumor-sorted $CD45^-EpCAM^+$ primary HGSOC cells) or with NY-ESO-peptide using K562 cells lentivirally transduced to express HLA-A2 as artificial APCs (aAPC), at ratio of 5:1. Where indicated PMA was added to the co-culture at 10ng/mL to increase the IL-2 production. 48h

after seeding, the supernatant was harvested, and used for IL-2 detection using ELISA MAX™ Deluxe Set Human IL-2 (Biolegend) and absorbance at 450nm was measured with Gen5 Microplate reader and Image Software (Biotek).

Multiplex staining procedure

FFPE TMAs were immunostained using the PerkinElmer OPAL TM 7-Color Automation IHC kit (Waltham, MA) on the BOND RX autostainer (Leica Biosystems, Vista, CA) with the following anti-human antibodies: CD3 (ThermoFisher, SP7, 1:400, Thermo Fisher Scientific Cat# MA5-14524, RRID:AB_10982026), CD8 (DAKO, C8/144B, 1:100, Agilent Cat# M7103, RRID:AB_2075537), TCF1/7 (CST, C63D9, 1:100, Cell Signaling Technology Cat# 2203, RRID:AB_2199302), CD103 (Abcam, SP301, 1:100, Cat# ab227697), CD69 (Abcam, EPR21814, 1:300, Cat# ab233396), CLEC9A (Abcam, EPR22324, 1:100, Cat#ab223188, RRID:AB_2884022), PCK (DAKO, M3515, 1:200, Agilent Cat# M3515, RRID:AB_2132885). DAPI was used to stain nuclei. Tissues were heated at 65°C for 2h then transferred to the BOND RX (Leica Biosystems) followed by automated deparaffinization and antigen retrieval using OPAL IHC procedure (PerkinElmer). As a negative control autofluorescence slides were included. Slides were scanned and imaged with the PerkinElmer Vectra®3 Automated Quantitative Pathology Imaging System. For quantitative image analysis multi-layer TIFF images were exported from InForm (PerkinElmer) and loaded into HALO (Indica Labs, New Mexico). Each fluorescent fluorophore was assigned to a dye color and positivity thresholds were determined per marker based on published nuclear or cytoplasmic staining patterns.

Spatial analysis for proximity analysis

For proximity analysis, we measured how many TRM-like cells ($CD3^+CD8^+CD103^+CD69^+$) were within 50μm of a dendritic - CLEC9A positive cell (DC). Then, the analysis was repeated to measure how many re-circulating TILs ($CD3^+CD8^+CD69^+CD103^-$) were within 50μm of DC. Finally, a third proximity analysis to measure how many re-circulating TILs ($CD3^+CD8^+CD103^-$) were within the same distance. We repeated the analysis for DCs located within stroma vs tumor islets. The total number of interactions (counts) between DCs and each of the other populations were considered 100%. From that, we estimated the percentage of interactions between DC-TRM-like, DC-recirculating ($CD3^+CD8^+CD69^+CD103^-$) and DC-re-circulating ($CD3^+CD8^+CD103^-$) TILs separately for stroma and tumor islets.

Spatial analysis and spatial association network

Spatial model fitting was conducted using the *spatstat* package for the R programming language (Baddeley and Turner, 2005). For each sample, the cell positions and phenotypes were used to create a marked point pattern dataset, and a convex hull was used to define the observation window for each TMA core. The original units of the datasets were pixels, but the unit was rescaled to be 1 μm. The set of 118 samples was treated as a replicated point pattern, allowing us to create a single interaction network that describes all samples (Baddeley and Turner, 2006).

Multitype Strauss hard core processes require the estimation two irregular parameters: hard core radii and interaction radii. Hard core radii were determined for each core by finding the minimum interpoint distances between each pair of cell phenotypes in that core(Baddeley and Turner, 2006). Interaction radii for each core were estimated by finding the radii that maximized the pseudolikelihood of a multitype Strauss hardcore process model fit to that core's point pattern dataset, as described in (Baddeley and Turner, 2006).

Following the estimate of the irregular parameters, each core was thus associated with a point pattern dataset, a matrix of hardcore radii, and a matrix of interaction radii. A single multitype Strauss hardcore process was then fit to all cores, using each core's associated point pattern dataset, interaction radii, and hardcore radii.

Community detection was performed on the fitted interaction, using the Leiden community detection algorithm (one graph of positive interactions, and second graph of negative interactions) (Mucha et al., 2010; Traag et al., 2019). Before community detection was performed, the interaction network was adjusted to be 1-interactions, as hardcore Strauss coefficients less than 1 indicate spatial repulsion, thus making spatial repulsion have negative values, and spatial attraction positive values.

Spatial clustering and t-distributed Stochastic Neighbor Embedding (t-SNE)- We extracted cell segments per core to build a count matrix with cells as rows and known phenotypes as columns. The known phenotypes are defined as follows: TRMstem ($CD3^+CD8^+CD69^+CD103^+TCF1^+$), TRMnon-stem ($CD3^+CD8^+CD69^+CD103^+$ $TCF1^-$), naïve re-circulating ($CD3^+CD8^+CD69^-CD103^-$) and recently activated re-circulating ($CD3^+CD8^+CD69^+CD103^-$) TILs.

A Euclidean distance matrix of dimension cells x cells is generated from this count matrix to compute the neighboring cells for each cell. We then build a spatial neighborhood for each cell where the phenotype expression of each cell is the average of six of its spatially nearest neighbors in Euclidean space. The Cellular Neighborhood approach is inspired from (Schurch et al., 2020), and the subsequent clustering is performed using a Gaussian mixture model to extract heterogeneous cell types. In this manner, we can extract clusters that are both spatially distinct and functionally similar. In effect, a sample can be viewed as a collection of such cellular neighborhoods where the same functional cluster can exist in multiple spatial locations.

The differentially expressed phenotypes used to annotate each cell type are those phenotypes with the highest z-score values for the log-normalized expression per cell type. The cells are further embedded in reduced 2D space using tSNE (Kobak and Berens, 2019).

QUANTIFICATION AND STATISTICAL ANALYSIS

Statistical details of experiments, number of repeats performed, and statistical tests used can be found in the figure legends or in method details of STAR Methods. Unless mentioned otherwise, all data presented shows mean with SEM (standard error of the mean). Two-tailed t-tests (Unpaired or paired, as appropriate) were performed unless indicated otherwise.

Survival analysis was performed by two-sided log-rank (Mantel–Cox) considering ≥ 3 and up to 60 months. Analysis and visualization were carried out in Graph Pad Prism 9.1.1 software. A significance threshold of 0.05 for P values and FDR-adjusted P value was used and P-values are denoted with asterisks as follows (*$p<0.05$, **$p \leq 0.01$, ***$p \leq 0.001$).